An efficient pressure-based multiphase finite volume method for interaction between compressible aerated water and moving bodies

van der Eijk, Martin; Wellens, Peter

Important note
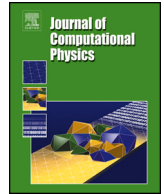To cite this publication, please use the final published version (if applicable).
Please check the document version above.

An efficient pressure-based multiphase finite volume method for interaction between compressible aerated water and moving bodies

Martin van der Eijk [a], Peter Wellens [b],*

[a] *Deltares, Delft, the Netherlands*
[b] *Delft University of Technology, Mekelweg 2, 2628CD Delft, the Netherlands*

A B S T R A C T

Maritime structures in heavy seas can experience wave impact events with high loads. The loads can lead to structural failure and even loss of life. Wave breaking in said sea states causes air to be entrained in water as aeration cloads, remaining long enough to be transported and to play a role in the impulsive interaction with the structure. A small amount of air in water already forms a highly compressible mixture. Compressibility influences the magnitude of the impact loads.

A new cartesian grid method for compressible multiphase flow is introduced to account for water, air and homogeneous mixtures of air and water. The method is designed to predict the hydrodynamic loads on moving bodies engaging with interfaces between fluids having large density ratios. An equation for conservation of energy is omitted by enforcing pressure-density relations. The interface between fluids is transported using a geometric Volume-of-Fluid method. The interface between fluids and structure is taken care of by a cut-cell method. An additional fraction field for the amount of air in water in combination with a new formulation for the multiphase speed of sound prevent overprediction of compressibility by artificial air entrainment. New experimental data of 2D wedge impacts with aerated water, made available as open data, are presented to demonstrate the validity of the numerical method. For low aeration levels, the simulation results in terms of the impact loads on the wedge and the frequencies of pressure waves generated upon impact are in good agreement with the experimental data. Increasing the level of aeration reduces the maximum impact load on the wedge. Reflected density waves lead to secondary loads on the wedge. The intensity of the secondary loads, relative to the primary load of impact, increases with the aeration level while the density wave frequency decreases.

1. Introduction

Maritime structures sail through heavy seas. Water waves encountered in these sea states can induce wave impacts on the structures and generate high loads. Wave loads have caused structural failure in the past [6,37,71,40]. In some cases, wave loads have led to loss of life [44,4].

Waves impact with structures like ships, quay walls, breakwaters and the side walls of containment tanks. The impulsive interaction between water and structure can also be represented by a structure that falls onto a free surface. A theoretical account of a falling

structure impacting with water is given by Von Karman [68]; experiments with this structure were performed by Greenhow [28]. Later work on impacts [70,78,42,27] has in common that the water was assumed incompressible.

Heavy seas feature breaking waves. Wave overturning causes air pockets to be enclosed, which break up under water to form clouds of air bubbles, that are only a fraction of a wave height in size. The small air bubbles remain entrained for several wave periods [64], the entrained air making up in the order of a percent of the water volume [7,55]. We refer to the process of air entrainment as aeration, and we call the mixture of water and air aerated water.

Due to aeration, the assumption of incompressibility of water is not always justified in modelling impulsive interaction of water with fixed structures [7,8,5,50,32]. Also for moving structures, experiments have demonstrated that aeration affects the results [48,49,23,24]. A small amount of air in water already leads to a significant increase in the compressibility of the mixture [75]. The compressibility of aerated water can cause the peak of the impact load to be smaller and the duration of the load to be longer, compared to impacts with water that can be considered incompressible. Compressibility also allows for the generation of density waves. These waves are defined as short-period oscillations of density and pressure propagating through the mixture with the speed of sound.

An early theory to account for compressibility with aeration was given by Peregrine and Thais [55] for a rapidly filling cavity, inspiring numerical methods for modelling aerated water impacts on structures. These methods show similarities to those for the prediction of cavitation erosion [63], vaporization [18], compressible wave impacts [46] and underwater explosions [51].

There is a scale difference of $O(10^4)$ and higher between a maritime structure and the aeration bubbles in the breaking waves that interact with the structure. A one-fluid formulation allows for coarser grids and likely has lower computational cost compared to methods in which every air bubble near the structure is resolved or tracked [10–12]. The implication of using a one-fluid formulation is that air bubbles move with the same speed as the water containing them. This is a reasonable model for the situation half a wave period after a wave near a maritime structure has broken.

A one-fluid, weakly-compressible method for modeling homogeneous mixtures of air and water was introduced by Bredmose et al. [6]. The method was based on the theoretical work of Peregrine and Thais [55]. The method solves for the conservation of mass (water and air), momentum, and energy. Aerated water is solved compressibly while the water remains incompressible in the energy equation. According to Ma et al. [47], the method features significant spurious oscillations in pressure and velocity near the interface between water and air. These oscillations are an artifact of a fully-conservative scheme [61] and can result in non-physical pressures and negative volumes of water [1].

The method proposed by Dias et al. [17] is similar to the method of Bredmose et al. [6]. It was designed for large aeration levels, omitting tracking or reconstruction of the interface between fluids. Oscillations in pressure and velocity were not present any more, but the fluid-fluid interface became so diffuse that the distinction between the compressible fluids disappeared. A diffuse interface may prevent oscillations, but it introduces a non-monotonic behavior of the speed of sound across the fluid-fluid interface when using the one-fluid assumption. Non-monotonic behavior is the spurious reduction in speed of sound near the interface between air and water causing erroneous pressure oscillations.

Ma et al. [47] introduced a Kapila-based model [39] being quasi-conservative to prevent the unphysical oscillations around the interface. The method is able to account for moving bodies and interface tracking using a cut-cell method and a Volume-of-Fluid method. A third-order MUSCL reconstruction was used for the interpolation of density values from cell centers to cell faces. A HLCC approximate Riemann solver was used for transporting convective fluxes. Comparison with experimental data of a flat plate entry in aerated water [48] validates that the method can predict the hydrodynamic loads involved in such an entry. At the same time, interface diffusion across several mesh cells for large flow gradient regions was reported.

The model proposed by Plumerault et al. [57] omitted the energy equation by using equations of state that describe the pressure-density relation. They introduced a new fraction field indicating the amount of air in water. A pressure-relaxation method is used to solve the system of equations. A pressure equilibrium is solved to compute the transport of the fluid-fluid interface, instead of solving a transport equation. Compared to the quasi-conservative model of Ma et al. [47], no assumption of the material derivative of entropy equal to zero is made. According to Ma et al. [47], the method of Plumerault et al. [57] is vulnerable to diffusion of the interface between fluids and to non-physical pressure oscillations at the density wave front, for similar reasons as for the method of Bredmose et al. [6].

Others accounts of the effect of aeration are Elhimer et al. [23] and Hong et al. [35]. These are left out of the discussion due to significant differences in modeling but do contribute to the overview of existing literature made here.

The objective of this article is to introduce an efficient, quasi-conservative consistent numerical method for modeling the interaction between homogeneous aerated water and maritime structures. We are mainly aiming at quantifying how aeration affects the impact loads on arbitrarily-shaped structures in the presence of a complex configuration of the interface between fluids. A secondary interest pertains to the effect of density waves on the hydrodynamic load, i.e. capturing the pressure oscillations as a result of reflecting and refracting density waves rather than resolving the discontinuity of density at the density wave front in the greatest detail. The following can be considered novelties:

- compared to Bredmose et al. [6], Plumerault et al. [57] and Ma et al. [47] that have a diffuse interface between fluids, the interfaces are kept sharp by means of a Volume-of-Fluid (VOF) method and geometric reconstruction of the fluid-fluid and fluid-body interface so that the moment of impact and the impact load are represented accurately and the non-monotonic behavior is prevented;
- contrary to Plumerault et al. [57], a transport equation is solved for the additional volume fraction field so that, in future, the aeration level can vary near the free surface. At present, for verification purposes, the aerated water is homogeneous;
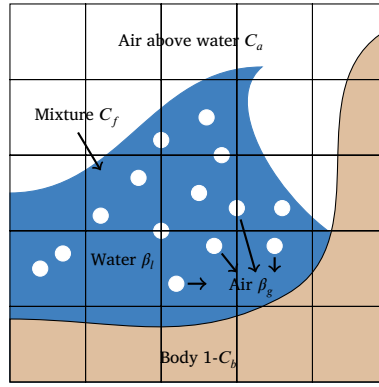
Fig. 1. Illustration of the phases of matter in the solver and how they are represented discretely in the cartesian grid. Volume fraction C_f is used for representing aerated water, C_a for air above the water, β_l for the water part of the homogeneous air-water mixture, β_g for the air part. C_b gives the part of a volume not occupied by the body and open to fluid.

- the speed of sound in the aerated mixture is adapted near the interface between fluids with respect to Wood et al. [76] to prevent a non-monotonic behavior of the speed of sound upon impact with bodies;
- contrary to Ma et al. [47] that formulated their methods as a density-based solver, the numerical method is set up as a pressure-based solver like those found for underwater explosions [51]. For low Mach numbers a pressure-based solver should be more efficient than a density-based solver, because the Courant number is not based on the speed of sound, but on the fluid velocities allowing for larger time steps. The oscillations at the disontinuity can be kept low by controlling the Courant number;
- benchmark experimental data for aerated water entries are rare. An experiment with wedge in aerated water were performed specifically for the purpose of validating the numerical method in this article. Where most investigations quantify only the effect of aeration on the magnitude of the primary impact peak, here also the post-impact, secondary loads from reflected density waves are considered.

The article starts with Sec. 2 introducing the variable definitions and the mathematical model in its conservative form. This mathematical model already begins with the assumption of a single fluid. The system of equations is closed by deriving the non-conservative formulation of the VOF transport equation and introducing pressure-density relations in Sec. 3. In Sec. 4 the grid structure is introduced, followed by Sec. 5 explaining the solution algorithm. In Sec. 6 the method is tested systematically against several benchmark 1D and 2D cases from literature. In Sec. 7 the wedge entry in aerated water is simulated and compared to the experiment that was set up specifically for validation of the method. The article ends with a summary of the conclusions.

2. Mathematical model

2.1. Interface capturing

'Free surface' is used interchangeably with 'interface'. Computing the position of the fluid-fluid and the fluid-body interfaces accurately is relevant for determining the moment of impact. A color function $f(\mathbf{x}, t)$ is used to capture the position of the interface. Transport of the interface is described by

$$\frac{Df}{Dt} = \frac{\partial f}{\partial t} + (\mathbf{u} \cdot \nabla) f = 0, \tag{1}$$

in which $f(\mathbf{x}, t) = 0$ gives the position of the interface and $\mathbf{u}$ the interface velocity.

A fixed Cartesian grid is used to divide the domain in volumes. We make use of an interface-capturing Volume-of-Fluid (VOF) method, in which the color function f is replaced by a discrete volume fraction field. A volume fraction is the average of the continuous color function for a given volume.

The definition of the volume fractions given in Fig. 1. Volume fraction C_b indicates the part of a volume that is open to fluid. 'Body' is used interchangeably with 'structure'. Fraction $(1 - C_b)$ then represents the part of a volume that is occupied by the body. Volume fraction C_a indicates the part of a volume that is occupied with gas (air), where C_f gives the part of the volume occupied with liquid, either water or aerated water, a homogeneous mixture of air and water.

Following Plumerault et al. [56], additional volume fraction fields are introduced to indicate the part by volume of the homogeneous mixture that is gas, β_g, and the part that is water, β_l. These volume fractions are necessary for the formulation of the mathematical model.

2.2. Fluids: conservative form

The governing equations for the mathematical model are formulated for a multiphase flow of immiscible Newtonian fluids. The one-fluid approximation is applied allowing for a single velocity and a single pressure field [52]. Equilibrium of pressure and a

no-slip boundary condition between fluids is applied, which is justified by the fact that our emphasis is on short-duration impacts with aerated water.

For the air in aerated water, we neglect bubble interaction and effects of surface tension. The air bubbles are assumed to be sufficiently small [74]. The assumption of a homogeneous air-water mixture is valid when the eigenfrequencies of the pressure waveguide due to compressibility are well below the bubble resonance frequency [75], so that the mixture effectively behaves as a single medium. When translated to our simulation setups, this is a requirement that is met in all cases. For long-duration events, the model requires an extension to deal with relative velocities between the fluids.

An equation for the conservation of mass, using a single velocity field $\mathbf{u}$, is formulated for each phase

$$\frac{\partial \alpha_k \rho_k}{\partial t} + \nabla \cdot \left(\alpha_k \rho_k \mathbf{u} \right) = 0, \quad k = a, l, g, \tag{2}$$

in which subscript a stands for air above water, l for the liquid part of the phase with aerated water, and g for the air part of the aerated water phase. Fractions α_k are defined as

$$\alpha_a = \frac{C_a}{C_b},$$
$$\alpha_l = \frac{\beta_l C_f}{C_b}, \tag{3}$$
$$\alpha_g = \frac{\beta_g C_f}{C_b}.$$

Refer to Fig. 1 for the definition of the volume fractions.

The equation for the conservation of mass for the aggregate fluid is obtained from the sum of the equations for each phase

$$\frac{\partial \rho}{\partial t} + \nabla \cdot (\rho \mathbf{u}) = 0, \quad \rho = \frac{C_b - C_f}{C_b} \rho_a + \frac{(1 - \beta_g) C_f}{C_b} \rho_l + \frac{\beta_g C_f}{C_b} \rho_a. \tag{4}$$

Parameter ρ is the aggregate fluid density that is used together with the algebraic relations

$$\beta_g + \beta_l = 1,$$
$$C_f + C_a = C_b, \tag{5}$$

Although not required, we now say that $\rho_g = \rho_a$ because for all our applications the gas entrained in water originates from the air above it.

The equations for the conservation of momentum, using again a single velocity field and a single pressure field read

$$\frac{\partial \rho \mathbf{u}}{\partial t} + \nabla \cdot (\rho \mathbf{u} \otimes \mathbf{u}) + \nabla p + \rho \mathbf{g} = 0. \tag{6}$$

Here, p is the pressure in the aggregate fluid and $\mathbf{g}$ the vector of the acceleration of gravity. Note that the viscous term has been omitted from the momentum equation as mainly short-duration events will be considered, in which viscous effects such as the formation of boundary layers can be ignored.

2.3. Body motion

The body is assumed rigid and is displaced by a state-space representation of Newton's second law. The position of the body $\mathbf{x}_b$ is found from

$$\frac{\partial \mathbf{x}_b}{\partial t} = \mathbf{u}_b, \tag{7}$$

and the body velocity $\mathbf{u}_b$, in turn, is found from

$$m_b \frac{\partial \mathbf{u}_b}{\partial t} = \mathbf{F}_b. \tag{8}$$

The mass of the body, m_b, is assumed constant. The force on the body, $\mathbf{F}_b$, includes the force of gravity and the force exerted by the fluid.

The fluid force on the body is found from integrating the pressure in the normal direction to the boundary along the body contour. Viscous stresses on the body, as said, and rotation of the body are not considered.

3. Closure of system of equations

3.1. Fluids: speed of sound

Sec. 2 described the system of equations consisting of three independent equations for the conservation of mass, equations for the conservation of momentum in the axis directions, and two equations for the state-space of the body. The pressure and velocity field

are solved from this system. But the system of equations is not yet closed as it is not yet been defined how to solve for the density field. That is described in this section, with due attention to closure of the system in three-phase points where air, aerated water and body meet as we consider this a novelty with respect to the existing literature.

Densities are obtained algebraically using equations of state. These equations depend on the pressure and make the connection between the continuity equation (4) and the momentum equation (6) so that the change of density in time can be solved for. The relation between pressure and density can be written in a general form using the speed of sound. The square of the speed of sound is the ratio of the change in pressure to the change in density. Assuming that changes are small and neglecting second order terms and higher, the equation of state for an individual fluid becomes

$$\frac{D\rho_k}{Dt} = \frac{1}{c_k^2}\frac{Dp}{Dt}, \quad k = a, l, g, \tag{9}$$

with c is the speed of sound, being the propagation rate of a pressure wave with infinitesimal amplitude through a fluid at rest. The derivatives are taken at constant entropy, implying an adiabatic process.

The conservation of mass equation in Eq. (4) contains an aggregate density field which needs to be solved. The equation is rewritten in Eq. (10) such that Eq. (9) can be used.

$$\frac{D\rho}{Dt} + \rho\nabla\cdot\mathbf{u} = 0, \tag{10}$$

in which the first term is the material derivative of the aggregate density ρ. The material derivative of the aggregate fluid cannot be replaced yet with Eq. (9). Additional explanation is needed for solving the aggregate density ρ and the material derivative of this density. Using Eq. (4), definitions for the air and water density, and the speed of sound c need to be formulated.

The material derivative of the aggregate density ρ in Eq. (10) is rewritten by substituting the formulation of the aggregate density in Eq. (4). The material derivatives of the individual fluids are replaced with Eq. (5). Accounting for the presence of the body through volume fraction C_b, the material derivative of the aggregate density becomes

$$\frac{D\rho}{Dt} = \frac{C_b - C_f}{C_b}\frac{1}{c_a^2}\frac{Dp}{Dt} + \frac{C_f}{C_b}\left(\frac{\beta_g}{c_a^2} + \frac{1-\beta_g}{c_l^2}\right)\frac{Dp}{Dt} + \frac{C_f}{C_b}\left(\rho_a - \rho_l\right)\frac{D\beta_g}{Dt} + \frac{1-\beta_g}{C_b}\left(\rho_l - \rho_a\right)\frac{DC_f}{Dt}. \tag{11}$$

The body is assumed rigid, resulting in $\frac{DC_b}{Dt} = 0$ and, therefore, not visible in Eq. (11). The remaining unknowns to be defined for the aggregrate fluid and its material derivative are:

- the speeds of sound in air and water, c_a and c_l (Sec. 3.2), and
- the pressure-density relation for air and water, ρ_a and ρ_l (Sec. 3.2), and
- the material derivatives of β_g and C_f near the interface between air and aerated water, and the calculation of β_g (Sec. 3.3).

Resolving these unknowns in the next sections will lead to an equation of state of the aggregate fluid and a formulation of the aggregate speed of sound c, rather than separate equations for the constituent fluids.

3.2. Fluids: equations of state

The air above water, $C_a = 1 - C_f$, and the air in aerated water, β_g, are assumed compressible and to undergo isentropic compression. The relation between density and pressure under these circumstances is [51]

$$\frac{\partial\rho_a}{\partial p} = \frac{1}{c_a^2} = \frac{1}{a_c\gamma}\left(\frac{p}{a_c}\right)^{\frac{1-\gamma}{\gamma}} \quad \text{with } a_c = \frac{p}{\rho^\gamma}, \tag{12}$$

in which γ is the ratio of specific heat of the gas at a constant pressure to its specific heat at a constant volume, and a_c the isentropic constant. Note that the right-hand side of Eq. (12) represents a relation for the speed of sound in air (c_a) and can be used for substitution in Eq. (11). The specific heat ratio for air is equal to 1.0 for isothermal conditions and 1.4 for adiabatic conditions. Peregrine and Thais [55] showed the choosing a value of either 1.0 or 1.4 for the coefficient makes little difference for the loads generated during an impact. An adiabatic process happens relatively fast compared to an isothermal process like the propagation of sound. There is no time for heat exchange making $\gamma = 1.4$ a good assumption.

A nonlinear relation between density and pressure is derived from Eq. (12) by integration using $a_c = p_0/\rho_{a,0}^\gamma$. The formulation for ρ_a is needed in the material derivative in Eq. (11) and the aggregate density in Eq. (10).

$$\rho_a = \rho_{a,0}\left(\frac{p}{p_0}\right)^{\frac{1}{\gamma}} \tag{13}$$

Here, $\rho_{a,0}$ represents a reference value for the density. It is there to prevent "drifting" of the density during a simulation [72]. The reference value is chosen equal to the initial density, which is chosen equal to the density at atmospheric pressure.

The water part of the aerated water, β_l, is assumed weakly-compressible. For weakly compressible fluids, the relation between density and pressure is [51]

$$\frac{D\rho_l}{Dp} = \frac{1}{c_l^2},$$

(14)

with c_l the speed of sound in water. The speed of sound in water is assumed constant and can be directly substituted in Eq. (11). The integration of Eq. (14) results in a linear relation between the density of the water and the pressure needed in Eq. (11) and Eq. (10) for the aggregate density.

$$\rho_l = \rho_{l,0} + \frac{1}{c_l^2} \left(p - p_0 \right),$$

(15)

in which $\rho_{l,0}$ is the initial density to be chosen equal to the density of water under atmospheric conditions. Considering water weakly-compressible in this way will have little influence on the impact loads we are interested in, because for the pressure range we expect, the volume change of air in aerated water will be much larger than the volume change of water in aerated water. Hence, the major part of the volume change of the aerated water can be attributed to the volume change of air. Nevertheless, accounting for the compressibility of the liquid at this moment may extend the suitability of the method to applications not currently envisaged. Sec. 7.2 features a reflection on the pressure range in our current applications.

3.3. Fluids: volume fraction transport

In order to transport the interface between fluids, it is necessary to transport the volume fraction fields C_f and β_g. Also the material derivative for these volume fractions, for use in Eq. (11), have not yet been derived.

The dominance of the inertial effects over buoyancy makes the assumption of a constant mass fraction μ_g valid. The mass fraction is the ratio of the mass of aeration over the mass of the mixture of water and air. The constant mass fraction μ_g is predefined by

$$\mu_g = \frac{\beta_g \rho_a}{m_f},$$

(16)

means that $\frac{D\mu_g}{Dt} = 0$. Here, m_f is the mass of mixture air and water equal to $\rho_f C_f$ times the volume of the grid cell. The mass fraction can be rewritten to solve β_g, needed for solving the aggregate density ρ

$$\beta_g = \frac{\mu_g \rho_l}{(1 - \mu_g)\rho_a + \mu_g \rho_l}.$$

(17)

Substituting Eq. (16) in $D\mu_g/Dt = 0$ in combination with Eq. (9) results in the missing formulation of the material derivative of β_g in Eq. (11)

$$\frac{D\beta_g}{Dt} = \beta_g \left(1 - \beta_g \right) \left(\frac{1}{\rho_l c_l^2} - \frac{1}{\rho_a c_a^2} \right) \frac{Dp}{Dt}.$$

(18)

As mentioned in the introduction, a non-conservative formulation of the transport equation for C_f needs to be derived to prevent difficulties with spurious oscillations around the interface [1]. A formulation like this is found by considering mechanical equilibrium, i.e. equilibrium of pressure and velocity, between fluids [52].

The transport of the air-water interface with C_f needs a different formulation than the conservative form in Eq. (1). As mentioned in the introduction, a non-conservative formulation of the transport equation needs to be derived to prevent difficulties with spurious oscillations around the interface [1]. This formulation is found by using the mechanical (pressure and velocity) equilibrium between the fluids [52]. Summing all mass equations like for Eq. (4), as in Eq. (2), and using Eq. (9) for every phase results in an equation for total mass balance

$$\frac{Dp}{Dt} = -\frac{C_b}{\frac{\beta_g C_f + (C_b - C_f)}{\rho_a c_a^2} + \frac{(1 - \beta_g)C_f}{\rho_l c_l^2}} \nabla \cdot \mathbf{u}.$$

(19)

Filling in the sum of the mass balance of a and l results in

$$\frac{DC_f}{Dt} = -C_f \nabla \cdot \mathbf{u} - C_f \left(\frac{\beta_g}{\rho_a c_a^2} + \frac{1 - \beta_g}{\rho_l c_l^2} \right) \frac{Dp}{Dt}.$$

(20)

Note the independence of C_b which is essential for under-or overpredicting compressibility of a mixture and the similar form as the Kapila's one-dimensional transport equation [39]. The equation has proved to be competent and easier to deal with than the fully conservative formulation [38,61]. The right-hand side of Eq. (20) assures that the material derivative of the phase entropy is zero in the absence of shock waves.

The material derivative of C_f in Eq. (20) is needed to solve the transport of aerated water, but also for the material derivative of the aggregate density in Eq. (11). Substituting the missing unknowns defined in Sec. 3.1 in Eq. (11) results in the final formulation of the material derivative of the aggregate density needed for solving the total mass balance
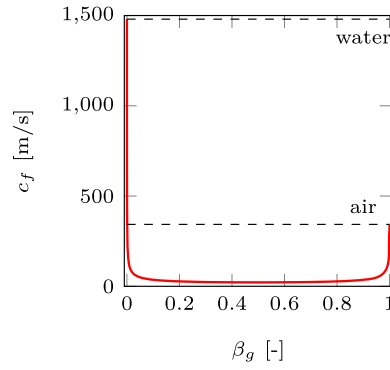
Fig. 2. Woods' formulation in Eq. (24) for mixture sound of speed c_f. Plotted for air volume fraction β_g assuming $C_f = 1$.

$$
\frac{D\rho}{Dt} = \rho \left(\frac{\frac{(1-\beta)C_f}{C_b}}{\rho_l c_l^2} + \frac{\frac{C_b - C_f}{C_b} + \frac{\beta C_f}{C_b}}{\rho_a c_a^2} \right) \frac{Dp}{Dt}. \tag{21}
$$

3.4. Fluids: mixture speed of sound

The final formulation of the material derivative of the aggregate fluid is known in Eq. (21). This means that, using Eq. (9), a formulation for the aggregate speed of sound is derived

$$
\frac{1}{\rho c^2} = \left(\frac{\frac{(1-\beta)C_f}{C_b}}{\rho_l c_l^2} + \frac{\frac{C_b - C_f}{C_b} + \frac{\beta C_f}{C_b}}{\rho_a c_a^2} \right). \tag{22}
$$

For the air-water mixture let's define a mixture density (ρ_f) by splitting the formulation in Eq. (4)

$$
\rho_f = (1 - \beta_g)\rho_l + \beta_g \rho_a, \quad \rho = \frac{C_f}{C_b}\rho_f + \frac{C_b - C_f}{C_b}\rho_a, \tag{23}
$$

where ρ_f is the density of the aerated water. According to [75], the speed of sound formulation for homogeneous mixtures

$$
\frac{1}{\rho_f c_f^2} = \frac{\beta_g}{\rho_a c_a^2} + \frac{1 - \beta_g}{\rho_l c_l^2} \quad \text{and} \tag{24}
$$

$$
\frac{1}{\rho c^2} = \frac{\frac{C_b - C_f}{C_b}}{\rho_a c_a^2} + \frac{\frac{C_f}{C_b}}{\rho_f c_f^2}. \tag{25}
$$

The mixture speed of sound formulation of Wood is illustrated in Fig. 2. Fig. 2 shows a large decrease in speed of sound for a small fraction of β_g, even up to values lower than the speed of sound of air c_a and water c_l at atmospheric conditions.

Compressibility factor

The trend in Fig. 2 can be explained by looking to the general formulation of the speed of sound [74]

$$
c_f = \frac{1}{\sqrt{\rho_f \kappa_f}}, \tag{26}
$$

in which κ_f is the compressibility factor for the mixture. Assuming the compressibility factor for air and density for water constant (C) for a low volume fraction β_g, $\kappa_f \approx \kappa_a$, and $\rho_f \approx \rho_l$ results in

$$
c_f = \frac{C}{\sqrt{\beta_g - \beta_g^2}}. \tag{27}
$$

Where the density hardly changes, the mixture has the compressibility of air.

3.5. Fluids: new formulation speed of sound

For the speed of sound around the interface where a clear distinction is between air and water, the mixture speed of sound formulation of Woods' does in reality not hold. There is no mixture between air and water at the fluid-fluid interface while we do
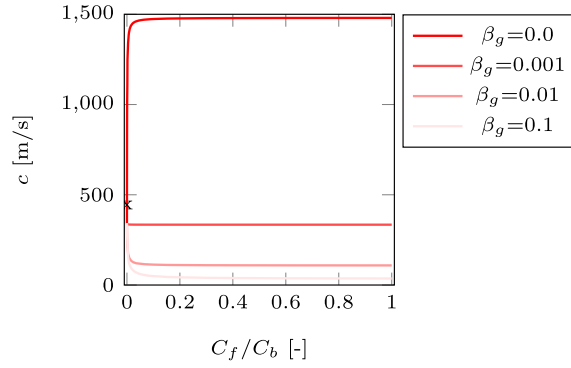
Fig. 3. Frozen speed of sound for different mixtures β_g, varying C_f over C_b. The cross represents the speed of sound of air.

use a homogeneous mixture model as stated in Sec. 2.2. The speed of sound at the interface is underestimated. The Woods' equation results in non-monotonic behavior and inaccurate wave transmission around the interface, getting worse for diffusive interfaces.

Ansari and Daramizadeh [2] gave another drawback for the mixture speed of sound relation in Eq. (25). The indicated problem is relevant for high-density ratio flows with large air volume changes and cavitation. The defined pressure-density relation in Sec. 3.1 can lead to negative densities when sub-atmospheric pressures play a role. A negative density results in a complex speed of sound for the mixture. As the introduction mentioned, aeration can lead to cavitation, meaning that the negative densities need to be prevented.

We decrease the effect of the non-monotonic behavior of the speed of sound across an interface by maintaining a sharp interface (explained in next Sec. 4). The consistent approach for determining the mass and momentum fluxes by [22] is used to deal with high-density ratio flows and sharp interfaces. The formulation of the air density by Wemmenhove [72] is used to prevent negative values when cavitation is involved. However, more attention needs to be paid when a rigid body, a cut-cell method, is involved.

Results in Sec. 6.4 showed that these measures were not enough when a body at the fluid-fluid interface is involved. The compressibility was not well predicted by comparing it with another numerical model. Saurel et al. [62] developed a formulation by adding an extra governing equation like the six-equations model of Hong et al. [34] to solve interface problems separated by compressible media. The corresponding formulation for the speed of sound is found called the frozen sound speed relation. This relation is the high-frequency limit of the particles with no mechanical equilibrium being the upper limit while the Woods' (mechanical equilibrium) speed of sound formulation is the lower limit. The particles are not able to adapt. Applying one of the two formulations was found to have small influence in the results [65]. In this paper we did find differences when a body was involved. By not assuming a homogeneous mixture around the interface, a transmitted pressure wave by the interface is better predicted.

The use of the frozen speed-of-sound formulation at the fluid-fluid interface solved the compressibility issue at the interface when a body is involved; around the body, and the interface between the mixture, C_f, and air, $(1 - C_f)$. The new formulation for the speed of sound replaces Eq. (22) in Eq. (11) with

$$\frac{1}{\rho c^2} = \frac{C_b}{C_f \rho_f c_f^2 + (C_b - C_f)\rho_a c_a^2} \tag{28}$$

where c_f is given by mixture speed of sound formulation in Eq. (24) for volume fraction β_g.

The authors are aware that changing the mixture speed of sound violates the mathematical derivation of the model in Sec. 3. The combination of the frozen speed of sound for volume fraction C_f and the mixture speed of sound for volume fraction β_g, including a body with two unique volume fraction fields is new. The behavior of the new formulation is illustrated in Fig. 3 and can be compared with Fig. 2.

4. Grid structure

Before introducing the discretization of the governing equations, the grid structure is introduced with the definitions and notations needed to solve the system of equations. A brief account is provided of how to identify the material interface between water and air, of the arrangement of variables being solved for within a grid cell, and of the cut-cell method to incorporate moving bodies. This account follows the lines of the method introduced by van der Eijk and Wellens [22].

A fixed 2D cartesian grid is employed to divide the domain in cells. Cell labeling is used to identify the position of the interface within the grid. As stated in the introduction, the method should maintain a sharp interface to reduce the nonmonotonic behavior of the speed of sound. Labeling aids in keeping the interface sharp because cells with air can be treated differently from cells with (aerated) water, and differently again from cells that contain the interface between air and (aerated) water. The cell labeling proposed by van der Eijk and Wellens [22] is used and illustrated in Fig. 4a. The choice of label is based on the volume fraction C_f. A cell completely filled by the body is labeled B and is not included in the system of equations. A cell without liquid ($C_f = 0$) is labeled E (empty, for historical reasons [41]). When a cell contains some fluid and is adjacent to an E-cell, it is given the S-label (surface).
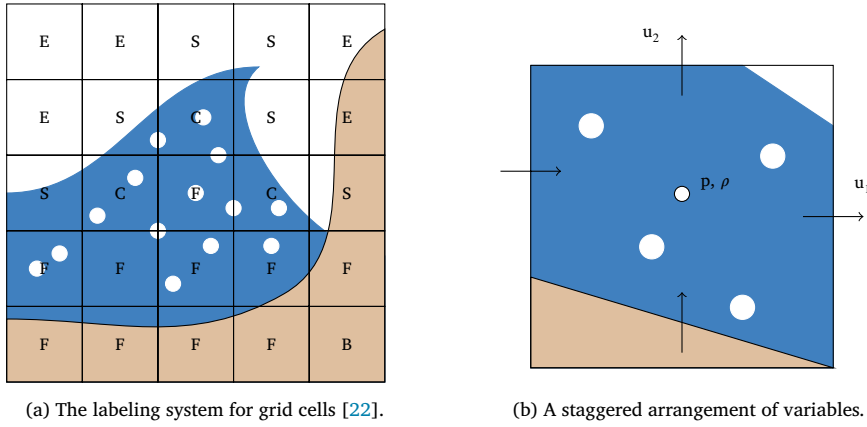
(a) The labeling system for grid cells [22].

(b) A staggered arrangement of variables.

Fig. 4. Fixed Cartesian grid structure with labels making a distinction between body, water, and air. Standard MAC configuration of variables (staggered); scalar variables (p and ρ) are defined in cell centers (○), the velocity field u is sampled at the faces of the cell (→).

A cell with some fluid and adjacent diagonally to one empty cell is labeled as C. Remaining cells are labeled F (fluid, again for historical reasons). A F-cell is not allowed to connect with an E-cell. Note that a F-cell is not necessarily completely filled.

The standard Marker-and-Cell (MAC) staggered arrangement of variables within a grid cell is used, meaning that the scalar variables (pressure p, density ρ, and volume fractions C_f, C_b, β_g) are positioned in cell centers, and the components of the velocity vector normal to the cell faces ($\mathbf{u} = [u_1, u_2]^T$) are positioned at those faces. The arrangement of variables is shown in Fig. 4b. Control volumes are employed to solve the governing equations. Two different kinds of control volume are used. Conservation of momentum is solved for in momentum control volumes, and continuity is solved for in mass control volumes. Mass control volumes coincide with grid cells, see Fig. 5a. Momentum control volumes lie staggered in the grid with respect to mass control volumes. All control volumes are shown in Fig. 5b. Averaging is needed to obtain values of the density at the positions of the velocity components. A consistent averaging procedure is described by van der Eijk and Wellens [22] and not discussed further here.

The body is represented using a cut-cell method [25]. A cell is called a 'cut cell' when part of the body's contour intersects with this cell. The part of the cell not occupied by body is referred to as volume fraction, or volume aperture, C_b. The interface between body and fluids cuts through the cell by means of piecewise-linear segments. Volume and face apertures are used to account for the presence of the body. Volume aperture C_b indicates the part of a grid cell's volume that is open to fluid. Face apertures a_b indicate the area of a grid cell's faces that is open to flow. Apertures are illustrated in Fig. 5a. Apertures scale the size of the control volumes so that the equations in cut cells are solved like those in uncut cells; the discretization of the equations does not change. A visual representation of the scaling of control volumes is given in Fig. 5b. The size of the mass control volume is $C_b \delta x \delta y$, and left-most part of the boundary of the control volume that is open to flow is $a_b \delta y$. More about the treatment of cut cells is given in van der Eijk and Wellens [22].

5. Discretization and solution algorithm

The governing equations for conservation of mass (4) and conservation of momentum (6) of the fluids are discretized and combined with the discrete representations of the equations of motion of the body (7) and (8) into a system of equations for solving the pressure p and the body velocity $\mathbf{u}_b$. The fluid velocities $\mathbf{u}$ are solved from the pressure gradients. The fluid and body velocities are used to transport the interface between fluids and the interface between fluids and body. Density ρ and the fraction of air in water β_g (aeration) are solved algebraically. The equations are combined into a solution algorithm.

The solution algorithm is an extension of the incompressible two-phase flow method in van der Eijk and Wellens [22], that uses the same discretization techniques for the mass, momentum and interface transport to obtain a consistent method. Without consistency, momentum losses and distortion of the interface are found for high-density ratio flows. A temporary continuity equation was used to obtain consistency, solving it on momentum control volumes to prevent momentum losses as a result of the staggered grid.

A one-step projection method [14] is used for solving the pressure. Time levels are indicated using superscripts $n+1$ and n. A $\sim$ above variables indicates an auxiliary step. The following discrete operators are used to compose the system of equations: Ω_f, Ω_c. $\mathfrak{C}_f$, M_c, M_f, $\mathcal{A}_c$, $\mathbf{I}$, in which subscript (f) or (c) is used to indicate whether the operator is applied on momentum or mass control volumes respectively. The symbols represent the discrete

- M: divergence operator, that depends on grid sizes and face apertures a_b [25].
- M^T: transpose of the divergence operator that equals the negative gradient operator, working on pressures that are considered constant within grid cells [13].
- $\mathfrak{C}$: convective operator that retains the skew-symmetry of its continuous counterpart [67].
- Ω: volume operator representing the grid cell volume scaled by C_b [25].
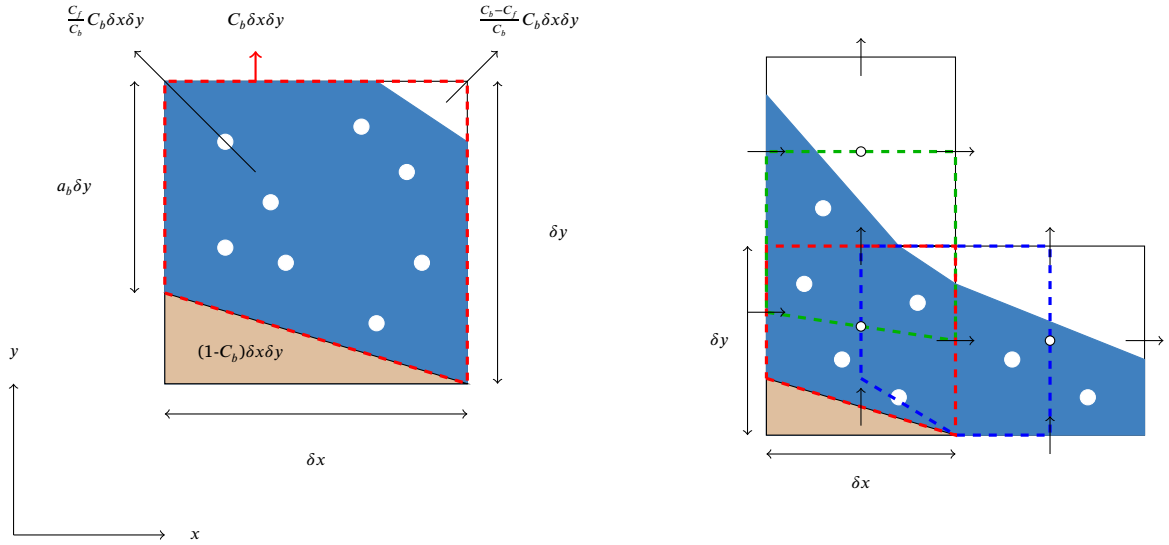
(a) Cut cell with volume aperture C_b indicating the part of the grid cell's volume open to fluid and face aperture a_b indicating the area of a grid cell's face open to flow. The mass control volume is shown as (—). The filling ratio of cells is administered in terms of C_f and C_b.

(b) Staggered arrangement of control volumes within the grid. Mass control volumes coincide with grid cells.

Fig. 5. Control volumes and cut cells. Cut cells are used to represent arbitrarily shaped moving bodies in the grid by means of piecewise-linear segments. Cut cells scale mass control volumes (—) and momentum control volumes with an averaging procedure, leading to this graphical representation of control volumes. Vertical momentum control volumes (—), and horizontal momentum control volumes (—) lie staggered with respect to mass control volumes.

- $\mathcal{A}$: operator that integrates the pressure along the body contour using face apertures a_b [22].
- **I**: identity matrix

The operators depend on time because of the volume and face apertures that change with the moving body.

The solution algorithm is explained as implemented.

FOR EACH TIME STEP

1. Solve volume fraction transport for fluid and body (C_f^{n+1}, C_b^{n+1}) and reconstruct interfaces with face apertures a_b^{n+1}
2. Solve auxiliary momentum field $\bar{\rho}\bar{\mathbf{u}}$ and ρ^n
3. Solve auxiliary density and vector field $\bar{\rho}$ and $\bar{\mathbf{u}}$
4. Solve vector field including all explicit terms $\tilde{\mathbf{u}}$ and ρ^{n+1} and β_g^{n+1}
5. Solve new pressure field with δp and coupling with body $\mathbf{u}_b^{n+1}$
6. Solve new fluid velocity field $\mathbf{u}^{n+1}$

After every time step, a Courant number is calculated for the new velocity field $\mathbf{u}^{n+1}$ [22]. When the Courant number does not satisfy the criterion associated with the time integration, the time step is halved until it does. When the Courant number is below a user defined minimum Courant number for 10 time steps, then the time step is doubled.

The following describes the discretization in order of the steps in the solution algorithm in subsections that have the same number as the step in the algorithm.

5.1. Interface transport

The interface capturing method consists of two steps: interface transport and geometrical reconstruction of the interface. Interface transport depends on the interface orientation and the discrete volume fraction field. The update for C_f is solved by means of the discrete representation of Eq. (20). The update for β_g is solved algebraically using Eq. (17). Transport equation (20) can be separated into an advective and a compressive part. For the advective part fluxes are computed along the boundary of a mass control volume. Fig. 6 shows a visual representation of a flux in a cut cell. Using fluxes, the discretization of the transport equation (20) becomes
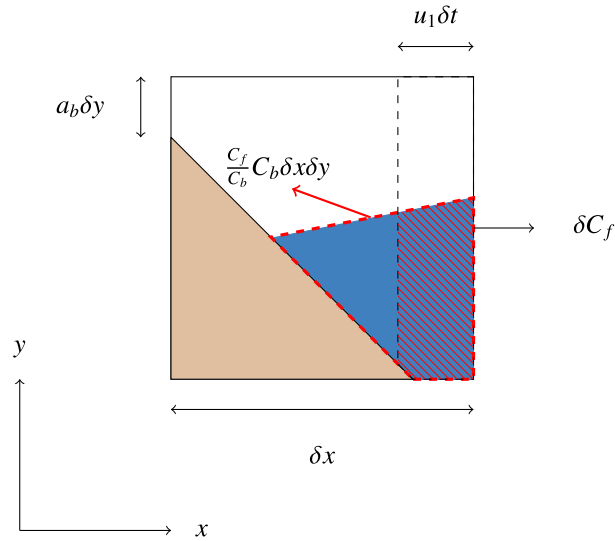
Fig. 6. Flux in a cut-cell near the interface between air and aerated water. The hatched area (—) represents the size of the flux δC_f. The area surrounded by the dashed line (—) represents the volume of the air-water mixture $\frac{C_f}{C_b}\delta x \delta y$ in the mass control volume.

$$C_f^{n+1} = C_f^n - \frac{1}{\delta x \delta y}\boxed{\sum_{sides} \delta C_{f,side}}^1 - \frac{\delta t}{\delta x \delta y}\boxed{\frac{C_f^n}{C_b^n}\left(\frac{\beta_g^n}{\rho_a^n \left(c_a^2\right)^n} + \frac{1 - \beta_g^n}{\rho_l^n \left(c_l^2\right)^n}\right)\frac{Dp}{Dt}}^2,$$

(29)

where the material derivative is discretized as in Sec. 5.5.

Boxed term 1 represents the advective part, boxed term 2 represents the compressive part. A flux δC_f is of the form

$$\delta C_f \propto \frac{C_f}{C_b}u_1 \delta t a_b \delta n,$$

(30)

with δn representing the cell face size which in 2D corresponds to either δx or δy. In the example in Fig. 6, δn is equal to δy.

There is existing literature about using reconstruction after transporting the interface, to good effect [53,69,15]. Geometric reconstruction reduces mass loss and keeps the interface sharp. The bilinear interface reconstruction method of van der Eijk and Wellens [19] is used. The labelling system in Fig. 4a is used for marking out cells where the interface needs reconstruction; those are cells labeled with S or C. An example of a PLIC interface segment is shown in Figs. 5a and 5b.

The body is displaced similarly to Eq. (29). The difference is that the compressive term does not need to be computed. The transport equation for the body is

$$C_b^{n+1} = C_b^n - \frac{1}{\delta x \delta y}\sum_{sides} \delta C_{b,side}.$$

(31)

After updating C_b to C_b^{n+1}, the interface between body and fluids is reconstructed using the same PLIC method that is used for the interface between fluids. The face apertures a_b^{n+1} indicated in Fig. 5a are found by averaging end points of the reconstruction lines in neighboring cells.

The motion of the rigid body is solved with a Eulerian method. It is not necessarily shape preserving, but in this way the same flux schemes are used for body and fluids, ensuring mass conservation. In addition, the mass fluxes of the fluids and body can be matched and made consistent, preventing momentum and mass losses [22]. Consistency is not guaranteed using the Lagrangian method and might require ad-hoc treatments.

5.2. Auxiliary momentum field

The momentum equation (6) is solved in steps. First, an auxiliary momentum field $\bar{\rho}\bar{\mathbf{u}}$ is solved for

$$\frac{\bar{\rho}\bar{\mathbf{u}} - \rho^n \mathbf{u}^n}{\delta t}\Omega_f^{n+1} + \mathfrak{C}_f^n\left(\rho^*\{\mathbf{u}^n, \mathbf{u}_b^n\}\right)\mathbf{u}^n.$$

(32)

Momentum $\rho^*\mathbf{u}$ is defined as the weighted average of momentum contributions from the two fluids that are modelled

$$\rho^*\mathbf{u} = (C\rho_f + (1 - C)\rho_a)\mathbf{u},$$

(33)

in which C is a weight that is based on the mass fluxes

$$C = \frac{|\delta C_f|}{|\mathbf{u}| a_b \delta t \delta n},$$

(34)

using δC_f from Eq. (30) to obtain consistency between mass and momentum.

Density field ρ^n is found using the values of p^n, C_f^n and C_b^n and the reconstruction of the interface from the mass control volumes that have overlap with the momentum control volume under consideration using the definition in Eq. (4). When the pressure at the position of a velocity in a cell is necessary, it is found as the average of the two nearest pressures in the direction of that velocity.

5.3. Auxiliary density

An auxiliary density field $\bar{\rho}$ is computed for the momentum control volume that complies with the discretization of the momentum fluxes and VOF fluxes by means of a temporary continuity equation. The auxiliary density field is needed due to the inconsistency between ρ^{n+1} and $\bar{\rho}$ [22,59,9]. The temporary continuity equation reads

$$\frac{\bar{\rho} - \rho^n}{\delta t} \Omega_f^{n+1} + M_f^n \left(\rho^* \{ \mathbf{u}^n, \mathbf{u}_b^n \} \right) = 0,$$

(35)

using the following approach near the interface between fluids and body

$$M_f^n \left(\rho^n \{ \mathbf{u}^n, \mathbf{u}_b^n \} \right) = M_f^n \left(\rho^n \mathbf{u}^n \right) + \left(1 - M_f^n \right) \left(\rho^n \mathbf{u}_b^n \right).$$

(36)

An auxiliary vector field $\bar{\mathbf{u}}$ is computed by dividing the auxiliary momentum field by the auxiliary density found from Eq. (35).

5.4. New density & new aeration fields

A second auxiliary velocity field $\tilde{\mathbf{u}}$ is constructed to contain the remaining terms of the momentum equation, that are integrated explicitly in time

$$\tilde{\mathbf{u}} = \bar{\mathbf{u}} - \delta t \left(\Omega_f^{n+1} \right)^{-1} \left(\frac{1}{\rho^{n+1}} \left(M_c^T \right)^{n+1} p^n + \mathbf{g} \right),$$

(37)

in which the new pressure field p^{n+1} is split into a temporal change δp and the pressure field at the old time level p^n.

Density field ρ^{n+1} is computed similarly to ρ^n. However, the new pressure field p^{n+1}, needed for equations of state of the fluids described in Sec. 3.1, remains as of yet unknown. In order to prevent having to iterate between density and pressure until convergence, which would involve a significant computational effort with solving a Poisson equation at every iteration, rather an auxiliary pressure field $\tilde{p}$ is constructed. Even without iterating between density and pressure, the Poisson equation in the current method described here constitutes 90% of the total computational cost. The auxiliary pressure field is found from

$$\frac{\tilde{p} - p^n}{\delta t} \Omega_f^{n+1} + M_c^n \left(p^n \{ \mathbf{u}^n, \mathbf{u}_b^n \} \right) - \left(p^n - \rho^n \left(c^2 \right)^n \right) M_c^n \left(\{ \mathbf{u}^n, \mathbf{u}_b^n \} \right) = 0.$$

(38)

Note that this equation is solved on mass control volumes. Then, using Eqs. (12) and (15) for the air density ρ_a^{n+1} and liquid density ρ_l^{n+1}, respectively, the new density field ρ^{n+1} is computed. The densities ρ_a^{n+1} and ρ_l^{n+1} are functions of p^*, but also of C_f^{n+1} and C_b^{n+1}, see Sec. 5.2.

The new aeration field β_g^{n+1} is computed using the new density values ρ_a^{n+1} and ρ_l^{n+1}, together with Eq. (17) in which the mass fraction μ_g is required to remain constant.

5.5. Pressure equation & coupling with body

The equation for the pressure change δp is obtained by taking the divergence (M_c) of the momentum equation and substituting it into the continuity equation by eliminating the velocity field at the new time step $\mathbf{u}^{n+1}$. The discrete continuity equation for a mass control volume equals

$$\frac{1}{\rho} \frac{D\rho}{Dt} + M_c^{n+1} \left(\{ \mathbf{u}^{n+1}, \mathbf{u}_b^{n+1} \} \right) = 0.$$

(39)

After substituting the discrete momentum equation into Eq. (39) and rearranging terms, an equation for δp and $\mathbf{u}_b^{n+1}$ is obtained

$$\delta t M_c^{n+1} \left(\Omega_f^{n+1} \right)^{-1} \frac{1}{\rho^{n+1}} \left(M_c^T \right)^{n+1} \delta p - \left(1 - M_c^{n+1} \right) \mathbf{u}_b^{n+1} = M_c^{n+1} \tilde{\mathbf{u}} + \frac{1}{\rho} \frac{D\rho}{Dt}.$$

(40)

The material derivative density term in Eq. (40) is solved with Eq. (21)

$$\frac{1}{\rho} \frac{D\rho}{Dt} = \frac{1}{\rho^{n+1} \left(c^2 \right)^{n+1}} \left(\frac{\delta p}{\delta t} \Omega_c^{n+1} + M_c^{n+1} \left(p^n \{ \tilde{\mathbf{u}}, \tilde{\mathbf{u}}_b \} \right) - p^n M_c^{n+1} \{ \tilde{\mathbf{u}}, \tilde{\mathbf{u}}_b \} \right),$$

(41)

from which the unsteady term with the pressure change δp needs to be moved to the left-hand side of Eq. (40). How the speed of sound (c) is computed is described in Sec. 3.5.

The discrete representation of the equations of motion of the body Eq. (8) is given by

$$\frac{\mathbf{u}_b^{n+1} - \mathbf{u}_b^n}{\delta t} m_b + m_b \mathbf{g} + \mathcal{A}_c^{n+1} \left(\delta p + p^n \right),$$ (42)

in which $\mathcal{A}_c$ is an operator that integrates the pressure over the surface of the body. Similar to the auxiliary velocity and pressure fields, an auxiliary body velocity $\tilde{\mathbf{u}}_b$ is formulated including terms that are integrated explicitly

$$\tilde{\mathbf{u}}_b = \mathbf{u}_b^n + \delta t m_b^{-1} \left(m_b \mathbf{g} + \mathcal{A}_c^{n+1} p^n \right).$$ (43)

Fluids and body are coupled through the pressure. The following system of equations needs to be solved to find the field of pressure change δp the body velocity $\mathbf{u}_b$

$$\begin{bmatrix} \mathcal{L}_p & -M_b^{n+1} \\ \delta t m_b^{-1} \mathcal{A}_c^{n+1} & \mathbf{I} \end{bmatrix} \cdot \begin{bmatrix} \delta p \\ \mathbf{u}_b^{n+1} \end{bmatrix} = \begin{bmatrix} \mathcal{R}_p \\ \tilde{\mathbf{u}}_b \end{bmatrix},$$ (44)

in which

$$\mathcal{L}_p = \delta t M_c^{n+1} \left(\Omega_f^{n+1} \right)^{-1} \frac{1}{\rho^{n+1}} \left(M_c^T \right)^{n+1} - \frac{1}{\rho^{n+1} \left(c^2 \right)^{n+1}} \delta t^{-1} \Omega_c^{n+1}, \text{ and}$$

$$\mathcal{R}_p = M_c^{n+1} \tilde{\mathbf{u}} + \frac{1}{\rho^{n+1} \left(c^2 \right)^{n+1}} \left(M_c^{n+1} \left(p^n \{ \tilde{\mathbf{u}}, \tilde{\mathbf{u}}_b \} \right) - p^n M_c^{n+1} \{ \tilde{\mathbf{u}}, \tilde{\mathbf{u}}_b \} \right).$$ (45)

5.6. New fluid velocity field

Finally, after having solved for the pressure change and the body velocity, the new fluid velocity field is computed from

$$\frac{\mathbf{u}^{n+1} - \tilde{\mathbf{u}}}{\delta t} \Omega_f^{n+1} + \left(M_c^T \right)^{n+1} \delta p = 0.$$ (46)

5.7. Reflection on discretization schemes

In this section the time integration has been represented as implicit for the pressure and Forward Euler for the explicit terms. This was for the purpose of presenting an already complex combination of equations, and in the presentation we wanted to keep emphasis on the equations and not confound matters with the details of the discretization. The algorithm as presented works, but improvement with respect to the presented algorithm can be obtained with the discretization discussed here.

The convective term in Eq. (32) is solved on a momentum control volume. This term is discretized using the high-resolution scheme [77,33]. The high-resolution scheme combines high-order accuracy with monotonicity and switches from second-order to first-order upwind near the interfaces between body and fluids and between fluids. An explicit second-order Adams-Bashforth time stepping scheme then is employed for the convective term to allow for larger time steps. The suitable Courant restriction for the combination of these two schemes is 0.25 or lower [72].

The material derivative of the pressure is solved on mass control volumes. The advective term of the derivative is split into two terms as illustrated in Eq. (41). The divergence term of the pressure is discretized using arithmetic averaging of pressures. The pressure equation in Eq. (44) is solved monolithicly to prevent instabilities that occur when the body mass is of similar order as the added mass [25]. When using a partitioned approach for fluids and body, a similar procedure as in Banks et al. [3] or in Roenby et al. [60] can be adopted. The equations of motion of the body are integrated in time using the Crank-Nicolson scheme [22].

The material interfaces defined using volume fractions C_f and $1 - C_b$ are transported using a direction-split scheme called COSMIC [45]. The COSMIC scheme is applied for the advective term in Eq. (29). A correction around the interface [73] is used to conserve mass for incompressible flows.

A final note on the discretization is that it was not designed to be completely mass conserving. It is quasi-conservative in which mass errors are carefully balanced against momentum errors and other errors that can be expected on the fairly coarse grids that cannot be avoided for the envisioned application of wave impacts on structures at sea. It is demonstrated next that the errors are well behaved and that the numerical results show good agreement with analytical solutions and experimental results.

6. Verification and validation with results from existing literature

Peregrine et al. [54] showed that it is likely that density waves are formed in the compressible medium after wave impacts of aerated water against structures. The capability of our method to represent the propagation of density waves is investigated by comparing with results of existing benchmark tests with compressibility from literature: a shock tube, a piston and a 2D shock bubble.

6.1. 1D shock tube

A shock tube is a 1D case in which a fluid or fluids at different initial pressure are separated before being released. The propagation of a density wave in a tube filled with air at different states initially was presented by van der Eijk and Wellens [20] using a similar
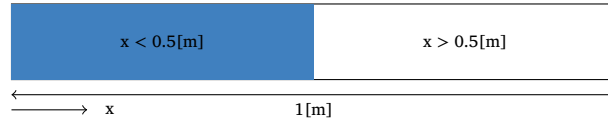
Fig. 7. Setup of simulation of a shock tube with water (blue) and air. Water initially at high pressure.

numerical method. Two shock tube cases are considered here. One with water at high pressure on one side of the tube and air on the other, and one with aerated water at a higher pressure one side of the tube than the other. Gravitational effects are not relevant and are omitted from the simulations. For both cases, three different grid resolutions are used and the effect of the Courant number on the results is evaluated.

6.1.1. Shock tube with two separated fluids

The first case resolves a density wave through a shock tube with two fluids, water and air. A shock tube with water and air was investigated analytically by Sod [66]. The setup of the simulation is illustrated in Fig. 7.

The fluid configuration, pressure and density satisfy the following initial conditions

$$C_f = \begin{cases} 1[\text{-}], & x < 0.5[\text{m}] \\ 0[\text{-}], & x > 0.5[\text{m}] \end{cases}, \quad p = \begin{cases} 1.0[\text{Pa}], & x < 0.5[\text{m}] \\ 0.1[\text{Pa}], & x > 0.5[\text{m}] \end{cases} \text{ and } \rho = \begin{cases} 1.0[\text{kg/m}^3], & x < 0.5[\text{m}] \\ 0.125[\text{kg/m}^3], & x > 0.5[\text{m}] \end{cases}.$$

The initial velocity field is zero. Aeration is not considered, so $\beta_g = 0$. As equations of state, these relations are employed

$$\rho_l = p, \quad \rho_a = \left(\frac{p}{a_c}\right)^{\frac{1}{\gamma_a}},$$

with ρ_l the density of water and ρ_a, $a_c = 1.34543$ and $\gamma_a = 1.25$ the density, specific heat ratio and isentropic constant for air, leading to the following expressions for the speed of sound in water and air respectively

$$\frac{1}{c_l^2} = 1, \quad \frac{1}{c_a^2} = \frac{1}{1.34543\gamma_a}\left(\frac{p}{1.34543}\right)^{\frac{1-\gamma_a}{\gamma_a}}.$$

The maximum Courant number, based on the instantaneous fluid velocities, equals 0.2. The final time for the simulations is set at 0.25[s]. Simulations are performed for several grid resolutions to investigate convergence. The resolutions are 250, 500, and 1000 cells over the tube length.

The simulation results are shown in Fig. 8 and compared to the analytical results of Sod [66]. The displacement of the interface between fluids is predicted well. The mass loss is never larger than 0.4% for the air phase and 0.01% for the liquid phase. A rarefaction wave propagates through the water in negative x-direction and a compression wave propagates through the air in positive x-direction. The fluid velocity is continuous across the interface between water and air. The velocity gradients in the rarefaction wave ($0.2 < x < 0.5$) are smoothed by numerical viscosity, which decreases with increasing grid resolution. Note that the compression wave front is not a formal discontinuity in the method; the velocity jump is smeared out over a couple of grid cells. The numerical viscosity is not sufficient to prevent wiggles near the compression wave front: small spurious velocity oscillations are found there that are independent of the spatial grid size; the wiggles are there because a shock-capturing method has not been applied and no amount of resolution is sufficient to resolve the discontinuity [29]. The velocity of the compression wave front is underestimated by 1.0% and also the fluid velocities are somewhat underestimated compared to the analytical results. This could be due to using the non-conservative form of the equations in the method. The non-conservative form does not satisfy the same Rankine-Hugoniot conditions, describing the states of the fluid on either side of the compression wave front, as the conservative form.

6.1.2. Shock tube with aerated water (water-air mixture)

The second case is a shock tube filled with aerated water, i.e. a homogeneous water-air mixture, with a higher pressure and density in the left-most half of the tube. An analytical solution for density wave propagation though dispersed fluids (mixtures) was reported in Franquet [26]. The assumption of homogeneity means that transport of the interface through C_f is not resolved; C_f is equal to one throughout the domain. The mass fraction of the air in water is $\mu_g = 1.31 \cdot 10^{-5}[\text{-}]$. The initial conditions for the air volume fraction associated with that mass fraction, and for the pressure on either side of the shock tube are

$$\beta_g = \begin{cases} 1.95 \cdot 10^{-3}[\text{-}], & x < 0.5[\text{m}] \\ 1.00 \cdot 10^{-2}[\text{-}], & x > 0.5[\text{m}] \end{cases}, \quad p = \begin{cases} 10^6[\text{Pa}], & x < 0.5[\text{m}] \\ 10^5[\text{Pa}], & x > 0.5[\text{m}] \end{cases}.$$

The initial conditions for the density of the air in water and for the density of the water are

$$\rho_a = \begin{cases} 6.91[\text{kg/m}^3], & x < 0.5[\text{m}] \\ 1.33[\text{kg/m}^3], & x > 0.5[\text{m}] \end{cases}, \quad \rho_l = \begin{cases} 1027.4[\text{kg/m}^3], & x < 0.5[\text{m}] \\ 1027.0[\text{kg/m}^3], & x > 0.5[\text{m}] \end{cases}.$$

The equations of state are the same as in Sec. 3.1.

At first a maximum Courant number based on the instantaneous fluid velocities of 0.001 is set. The final time of the simulations is $5.5137 \cdot 10^{-4}[\text{s}]$. Simulations with three grid resolutions are performed, using 250, 500 and 1000 cells in the length of the tube.

(A) Volume fraction field showing position interface between fluids.
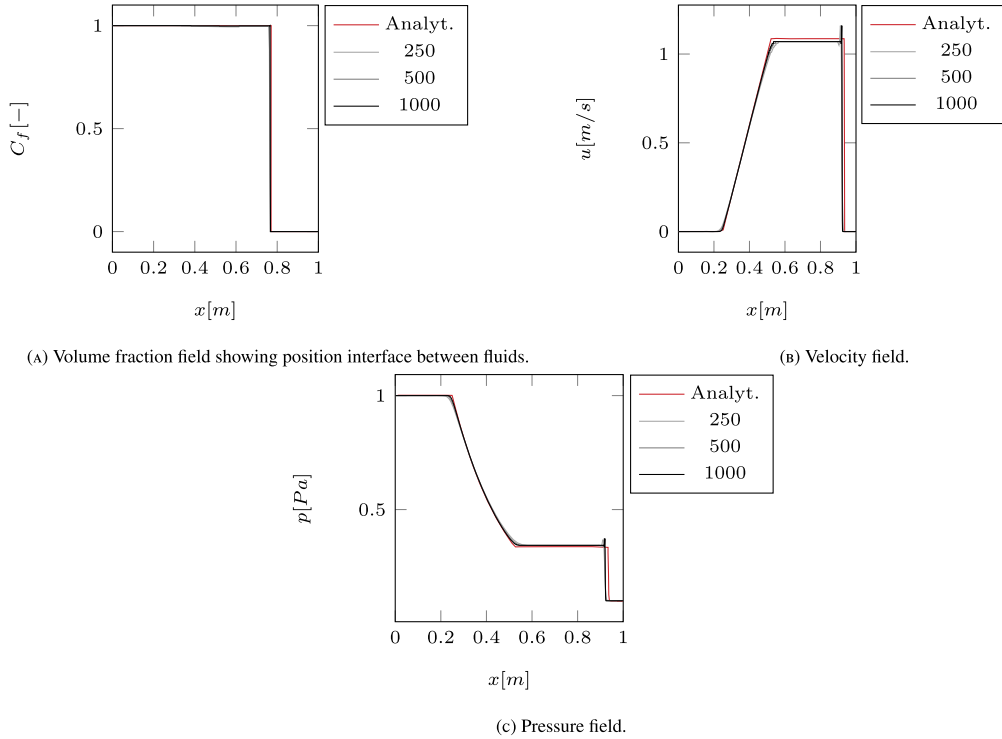

(B) Velocity field.

(c) Pressure field.

Fig. 8. Shock tube with water and air: numerical results compared to analytical solution [66] for three different grid resolutions at time $t = 0.25[s]$.

The results of the simulations are shown in Fig. 9. The results are in agreement with the analytical solution except at the discontinuity where wiggles are found because it is underresolved. At the discontinuity, the results will not converge to the analytical solution. However, convergence for the pressure signal is found for the L_1 and L_2 norm up to first-order and L_∞ above first-order.

The slight jump in the aeration and density field near $x = 0.5[m]$ is caused by a temperature fluctuation, which our method does not solve for. Similar observations as for the shock tube with water and air separately can be made regarding numerical viscosity, the resolution of velocity gradients and oscillations near the compression wave front.

Next, the effect of the maximum Courant number on the results is investigated. Simulations are performed in which the maximum Courant numbers are varied between $5 \cdot 10^{-4}$ and $1 \cdot 10^{-2}$ at a grid resolution of 1000 cells. The results are shown in Fig. 10, zooming in on the direct vicinity of the compression wave at time $t = 5.51 \cdot 10^{-4}[s]$. The resolution of the jump in velocity over the compression wave front is strongly affected by the choice for the maximum Courant number. With a Courant number of $5 \cdot 10^{-4}$ the jump is resolved well but velocity oscillations (wiggles) are observed. The oscillations become smaller for higher Courant numbers, until for a value of $5 \cdot 10^{-3}$ no oscillations remain. But at a maximum Courant number of $1 \cdot 10^{-2}$, the jump in velocity near the compression wave front is also not resolved well anymore.

For the shock tube with aerated water the speed of the propagating density wave is close to $200[m/s]$. That means that for a Courant number based on the fluid velocities of $5 \cdot 10^{-3}$, the Courant number based on the speed of the density wave is approximately 1. Considering the shock tube with separated water and air with a Courant number based on fluid velocities of 0.2, the Courant number based on the density wave speed is 0.3.

To obtain an adequate representation of the fluid properties on either side of the density wave front, the experience with the shock tubes gives us that the Courant number based on the speed of the density wave needs to be below 1.

Note that the numerical method is not intended for a complete representation of shock fronts, but for the representation of effects associated with compressibility in impacts between waves and structures, such as the pressure oscillations due to density waves through the compressible medium.

6.2. Water or rigid body piston

To demonstrate the method's performance at capturing low-frequency, low-velocity, large scale compression of fluids that are separated by an interface, vertical 1D 'piston' simulations are performed [47,16]. The piston is either a layer of water or a body initially placed in between two layers of air before releasing it to fall down due to gravity. The piston compresses the air below while gaining and losing inertia, after which the compressed air pushes the piston back up again. At these low velocities, the water piston, being weakly compressible, is expected to behave the same as the piston that is modelled as a moving body.

The piston simulation setup is shown in Fig. 11. The piston is hatched to indicate that it can either be a rigid body (C_b is transported) or water (C_f is transported). The initial air density is $1[kg/m^3]$, and the density of water and body is $1000[kg/m^3]$. The
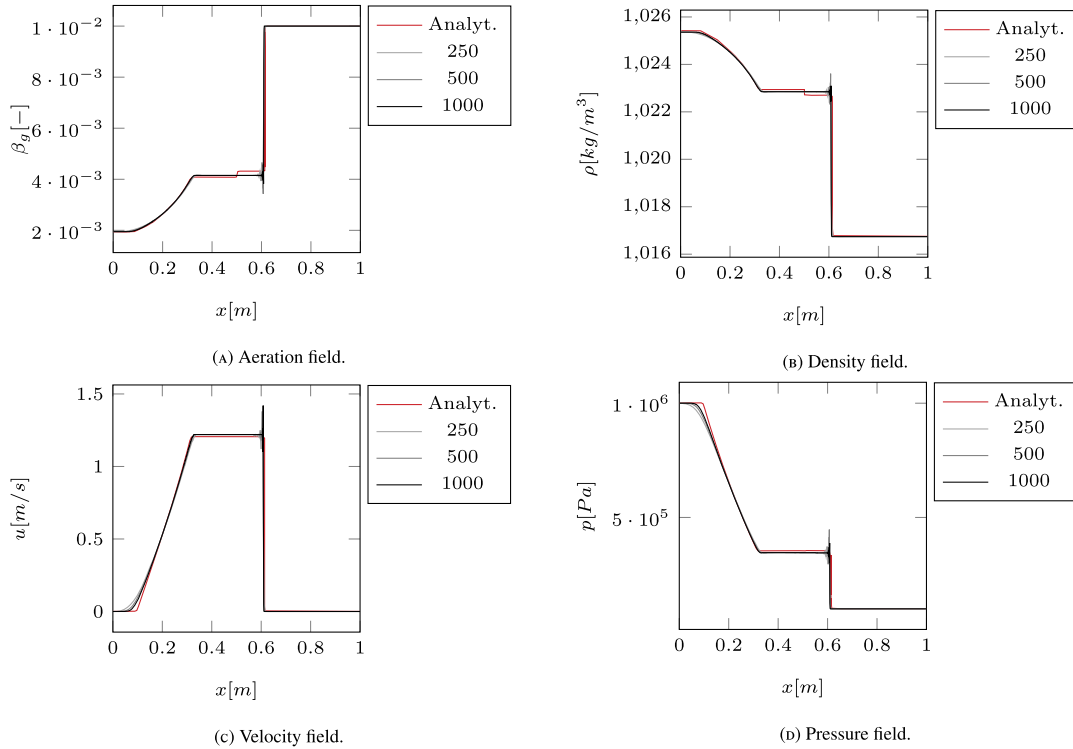
Fig. 9. Shock tube aerated water: numerical results compared with analytical solution [26] for three different grid resolutions at time $t =5.51\cdot10^{-4}$[s].
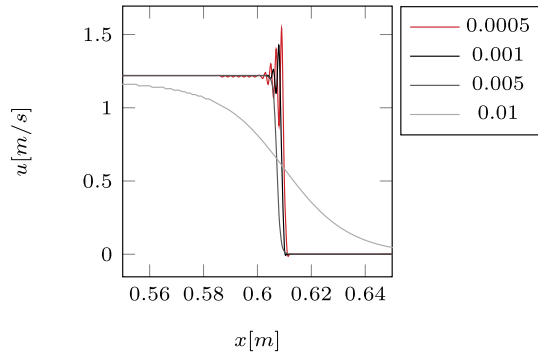

Fig. 10. Shock tube aerated water: effect of maximum Courant number (based on instantaneous fluid velocity) on the velocity on either side of the compression wave front. Simulations performed with grid 1000 and velocity shown at time $t =5.51\cdot10^{-4}$[s].

pressure follows an aerostatic pressure distribution with value of $1\cdot10^5$[Pa] at the bottom end of the domain. The gravity constant **g** is $[0, -9.81]^T$ [m/s^2]. The maximum Courant number is 0.2. The velocity field when the simulations start, is zero.

Results are given in Fig. 12 in terms of the pressure at the bottom end of the domain for different numbers of cells over the full height of the domain. Results are compared to those of Guilcher et al. [30]. The pressure over time with a piston composed of water in Fig. 12a has converged for grid 450 and then matches the results of Guilcher et al. [30]. The L_1, L_2, and L_∞ convergence rate found for the grid resolutions is above 2. When the water is replaced by a moving rigid body for grid 450, the pressure in Fig. 12b, the pressure is a match to that below the water piston. Both piston motions have the same expected physical behavior, even though the transport algorithms for C_f and C_b are quite different.

6.3. 2D shock bubble

The test case with a shock bubble is performed to investigate how density waves change direction and how they are transmitted between fluids in simulations with a compressible multiphase method. Helium shock-bubble experiments were performed by Haas and Sturtevant [31] and the results serve as a benchmark.
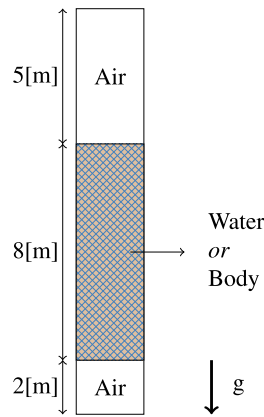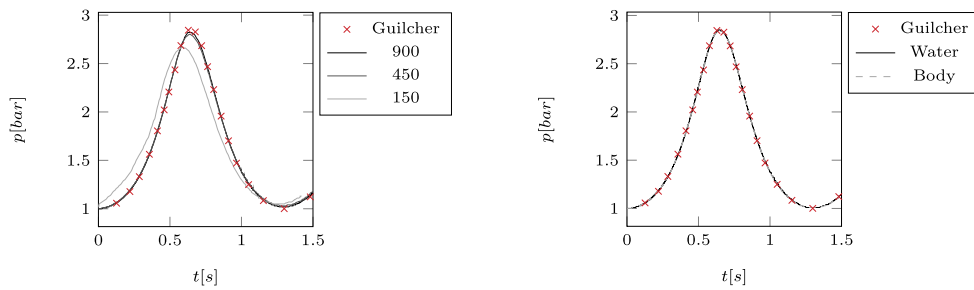
Fig. 11. Piston: simulation setup. Hatched area indicates either water or a moving rigid body.

(A) Pressure below water piston for different grids (maximum Courant number 0.2).

(B) Pressure below moving rigid piston compared to water piston for grid 450.

Fig. 12. Piston: pressure below piston as a function of time when piston is either water or moving rigid body.
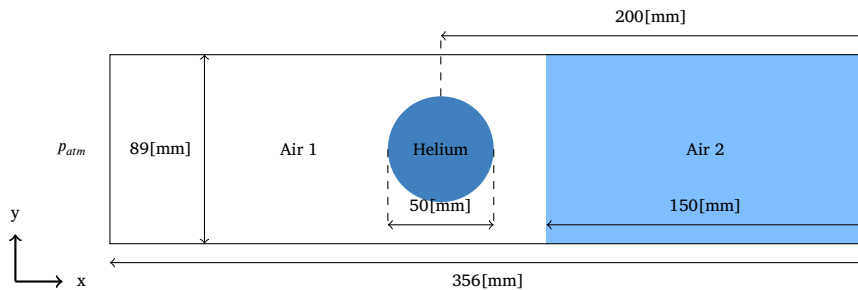

Fig. 13. Shock bubble: simulation setup with air at two states of pressure, and helium bubble in the air at one of these states.

The simulation setup for the 2D helium shock bubble case is illustrated in Fig. 13. Air, initially, is in two states on either side of the domain, just as for the shock tube. A cylindrical helium bubble is placed in the air at one of these states, approximately in the middle of the domain. The domain boundaries are closed with atmospheric pressure prescribed on the left horizontal end of the domain. Because the simulation setup is symmetrical in y-direction only half of the domain in that direction is simulated. Three grid resolutions are used in half of the domain: 1200x150, 800x100, and 400x50. A Courant number of 0.2 is used. The shock front arrives at the x-position of the helium bubble at $6 \cdot 10^{-5}$[s] after the fluids are released. From here on, the moment the shock front arrives at the position of the bubble is defined as $t = 0$[s].

The helium bubble in the experiment was contaminated with 28% air (of mass) [31]. The fluid properties in Table 1 take the contamination into account and are given for a temperature of 25 degrees Celsius [31]. These properties, according to the Rankine-Hugoniot equations, are associated with an initial shock front speed of 420[m/s] and a Mach number of 1.22 [31,58]. Quirk and Karni [58] conducted a detailed numerical study of the helium shock bubble. Kreeft and Koren [43] also simulated the shock bubble, but with different fluid properties using a density-based model solving Kapila's five-equation model for inviscid, non-heat-conducting, compressible two-fluid flows. Even though the fluid properties they used were different, the same shock front speed as in the experiment was obtained [43].

Table 1
Initial fluid properties for helium shock bubble simulation [31].

	γ [−]	ρ [kg/m^3]	p [kg/ms^2]	C_f [−]	β [−]	u [m/s]
Air 1	1.4	1.168	$1.0 \cdot 10^5$	1.0	0	0
Air 2	1.4	1.612	$1.5698 \cdot 10^5$	1.0	0	-115.5
Helium	1.648	0.212	$1.0 \cdot 10^5$	0	0	0
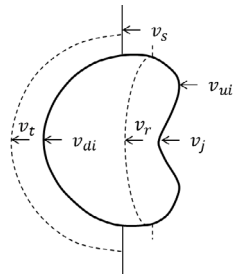
(A) Definition of interfaces and density wave fronts.
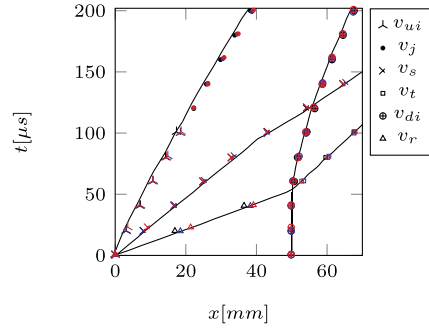
(B) Space-time plot of interface positions.

Fig. 14. Shock bubble: definition of interfaces and density wave fronts together with a space time plot of the position of the interfaces and wave fronts. Numerical results (markers) at three grid resolutions: 400x50 ■, 800x100 ■ and 1200x150 ■, compared with Quirk and Karni [58] (solid lines). The maximum Courant number is 0.2.

Table 2
Shock bubble: velocity magnitudes (in [m/s]) of interfaces and density wave fronts.

	v_s	v_r	v_t	v_{ui}	v_{di}	v_j
Haas and Sturtevant [31]	410	900	393	170	145	230
Quirk and Karni [58]	422	943	377	178	146	227
Kreeft and Koren [43]	419	956	-	176	-	-
Present model 1200x150 CFL=0.2	417	970	384	184	146	215

In the simulations, the front of the density wave before interacting with the helium bubble at t =0[s], is smeared out over ten grid cells. We chose the position in the middle of these 10 cells as the position of the density wave front to compare with the results from literature. The results of the simulations are given in terms of the positions and the velocities of the interfaces and the density wave fronts. The definition of all interfaces and shock fronts is given in Fig. 14a. Interfaces and shock fronts are identified by their velocities v. Fig. 14b features a space-time plot of the interfaces, in which the results of the numerical method at three grid resolutions are compared with the results of Quirk and Karni [58]. The maximum Courant number is 0.2. The results of our numerical method have converged, independent of how the discontinuity in the wave is solved. A convergence rate between the three grid resolutions of 1.3 is found. Where the grid spacing used by Quirk and Karni [58] was 0.056[mm], a relatively coarse grid is used in our simulations, with the 1200x150 grid having a spacing of 0.30[mm]. Spurious oscillations at the density wave front were not observed. Even at these coarse grids, the positions of the interfaces over time are in good agreement with Quirk and Karni [58]. A similar conclusion was found for the cases with the shock tube.

The velocity magnitudes of the interfaces and the density wave fronts are compared with the experimental results of Haas and Sturtevant [31] and the numerical results of Quirk and Karni [58] and Kreeft and Koren [43] in Table 2. Good agreement is found between the results of our method using grid 1200x150 (maximum Courant number 0.2) and the existing results from literature.

Fig. 15 shows density profiles at time t =$1.4 \cdot 10^{-4}$[s], taken at $y = 89$[mm] at the top of the domain and at $y = 49.5$[mm] in the middle of the domain, for grid resolutions 400x150 and 1200x150 and Courant numbers 0.005 and 0.2. Comparing results for the same Courant number, but different spatial grid resolution, and for the same spatial resolution but different Courant numbers, makes clear that increasing the spatial grid resolution and reducing the Courant number yield nearly the same effect: the density profile shows more variation and the density wave front is spread out less in space. The increase in grid resolution and the lowering of the Courant number did not significantly affect the position of the density wave front or the interface of the bubble themselves. The fluid interface between helium and air (at v_{di} and v_{ui}) is captured well and smeared out less due to the geometrical reconstruction.

6.4. 2D wedge entry in incompressible water

The test case of a 2D wedge impact with incompressible water is considered to evaluate the new speed-of-sound formulation in Eq. (28). The setup of the simulation is shown in Fig. 16a, containing the dimensions of the domain and the wedge; it is the same
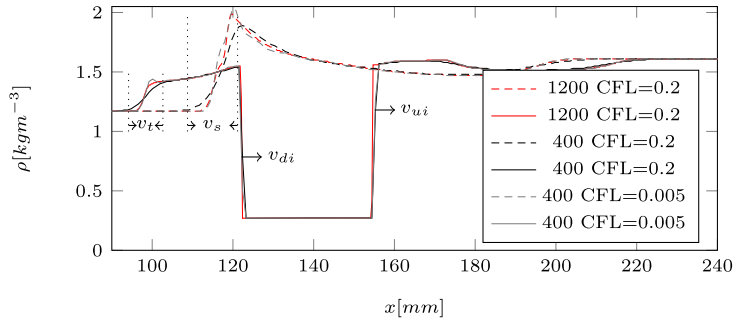
Fig. 15. Shock bubble: density profile ρ at time $1.4 \cdot 10^{-4}$ [s] for different grid resolutions and Courant numbers. Dashed lines for ρ at $y = 89$ [mm]. Solid lines for ρ at $y = 49.5$ [mm].
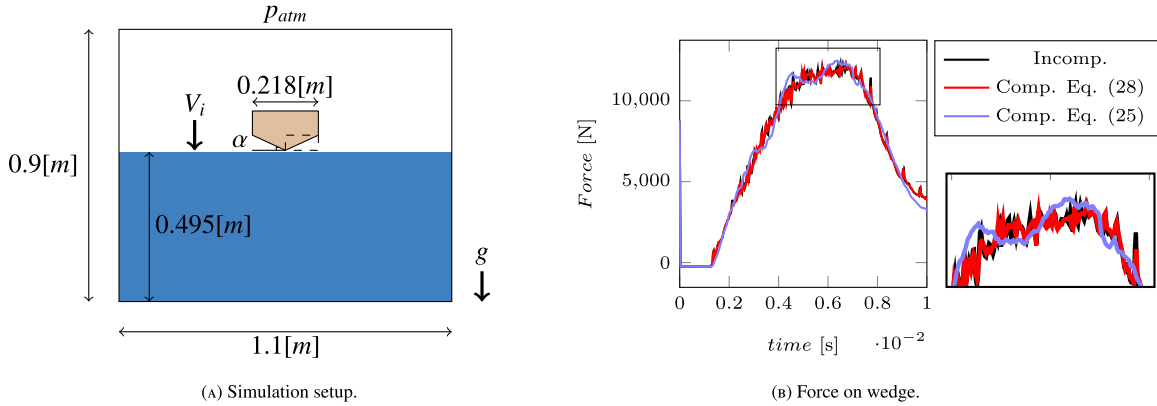

(A) Simulation setup.

(B) Force on wedge.

Fig. 16. 2D wedge entry: simulation setup and force on wedge as a function of time. Force from the current method with $\beta_g = 0.0$ and two different formulations for the speed of sound compared with incompressible model from an earlier article [20]. Grid 33x18 used.

setup as the one used in the next section about validation. The angle that the bottom planes of the wedge make with the horizontal, the so-called deadrise angle (α), is 15[deg]. In the simulation the wedge falls down vertically and impacts with the water. The vertical velocity of the wedge upon impact (V_i) is 7.0[m/s]. The grid is named for the number of cells that are used to represent the bottom plane of the wedge within the dashed box in Fig. 16a, because it is important to resolve the water jets formed in that box with sufficient accuracy. For the simulations described here, a grid resolution of 33x18 in the box is used.

Two simulations without aeration, so that $\beta_g = 0.0$, are performed, from which the vertical force on the wedge over time is obtained. Without entrained air in water, the results of these simulations should be close to that of the incompressible method described in van der Eijk and Wellens [20]. One simulation is performed with an implementation of the traditional mixture speed of sound in Eq. (25). The other simulation is performed with an implementation of the new formulation for the speed of sound in Eq. (28). Zooming in on the peak of the force in Fig. 16b, one finds that the force from the implementation with new speed of sound in Eq. (28) is a near-exact match with the force from the incompressible method [20]. The force from the implementation with the traditional mixture speed of sound in Eq. (25), shows a low-frequent oscillation. The low-frequent oscillation is the result of a numerical artifact that we call 'spurious compressibility'. In violent free surface flow, grid cells labelled F can sometimes receive a lower value for the filling ratio C_f than 1. Using Woods' equation, Eq. (25), values for $1 - C_f$ are treated the same as aeration, so that a fluid containing an artifact of violent free surface flow can become misrepresented as a compressible fluid. Small values for $1 - C_f$ can already lead to a significant decrease of the speed of sound. The spurious compressibility shows up as force oscillations some moments after the wedge impacts with the water. Eq. (28) corrects for the presence of F-labelled cells with values for C_f lower than 1 and therefore does not lead to force oscillations that should not be there.

7. 2D wedge impact with aerated water

In order to evaluate the capabilities of the numerical method in terms of fluid-structure interaction with compressible aerated water, it is validated against a new experiment that was performed specifically for this article. The data of the experiment will be made available as open data. Before motivating why it was necessary to conduct a new experiment, first an overview of existing literature about experiments with aerated water is provided.

7.1. Brief overview of experiments with aerated water

Experimental data for fluid-structure interaction with aerated water is rare [48,23,49,50,36], with Eroshin et al. [24] being an early account such an experiment. Ma et al. [48], Mai et al. [49], Hong et al. [36] used a flat plate and Elhimer et al. [23] used 3D cones with different deadrise angles. A general conclusion they made is that the effect of aeration is relevant for designing maritime structures operating in heavy seas. A significant reduction of the impact loads is found compared to impacts with pure water.

For flat plate impacts, Ma et al. [48] found that increasing the level of aeration increases the rise time and fall time of the impact pressure on the plate. They added that with flat plate impacts cavitation likely plays a role. Mai et al. [49], also studying flat plate impacts, motivated that the high-frequency oscillations associated with the compressibility of the medium they found, can have consequences for the fatigue analysis of the structure, but that the standard regulations for taking impact pressures into account may be conservative in the presence of aeration, as these, being based on pure water, specify impact pressures that are too high. Their results are in agreement with the numerical results of Hong et al. [36].

For cone impacts with aerated water, Elhimer et al. [23] found a reduction of the wetted contact surface, a reduction of the impact pressure, and a reduction of the average pressure, compared to cone impacts with pure water. They showed that the edge Mach number (Ma_{edge}) is relevant for indicating the significance of aeration on the peak pressures. The edge Mach number is the ratio of the fluid expansion velocity along the bottom of the body and the speed of sound of the mixture

$$Ma_{edge} = \frac{V_i}{\tan(\alpha)c_f}, \tag{47}$$

where c_f is found from Eq. (24) and α is the deadrise angle, that was illustrated in Fig. 16. Elhimer et al. [23] concluded that when the edge Mach number (Ma_{edge}) is above 0.05, compressibility has a relevant effect on the impact pressure. When Ma_{edge} is above 0.3, the type of nonlinearity related to that in the equation of state of the air-water mixture is found. In the range $0.05 < Ma_{edge} < 0.3$ the largest changes in impact pressures are found.

7.2. Experimental setup

The existing experiments in literature focus on finding the effect of aeration on the impact pressure. While that is certainly our motivation, too, validating the numerical method requires more than only the pressure. Because the speed of sound of the mixture has such a central role in the derivation of the closure model, the experiment for validation was designed to capture not only the pressure upon impact, but also the secondary pressure oscillations as a result of the reflected density waves. The body in the experiment is formed by a wedge, because the numerical method is not suited to capture the phase changes associated with the cavitation encountered by Ma et al. [48].

The setup of the experiment consists of three parts: the box containing water, the fall tower and the wedge attached to a guiding mechanism within the fall tower. The guiding mechanism prevents rotation. The error in orientation of the wedge due to tolerances between tower and guiding mechanism was investigated and found to be smaller than 0.1 degree. The fall height from the tip of the wedge to the initial free surface of the water is at most 2.83[m] so that, with friction, a maximum impact speed V_i up to 7.0[m/s] can be achieved. The box and wedge are illustrated in Fig. 17, in which α is the deadrise angle. The box is made of 36[mm] thick plywood, with a 30[mm] perspex front, having the overall inner dimensions of in-plane width×height×out-of-plane width=1100×900×240[mm]. The out-of-plane width of the wedge is 238[mm]. This is somewhat smaller than the box to prevent contact between wedge and box, while minimizing 3D effects due to the gap between wedge and box. The width of the wedge between chines is 218[mm], being five times smaller than the width of the box. The water level in the box is 495[mm] with respect to the bottom of the box.

Two wedges are used, each with a mass of 31.78[kg/m], having different deadrise angles (α). One has a deadrise angle of 15[deg], the other of 30[deg]. These deadrise angles are encountered frequently in industry at different cross-sections of high-speed vessels [21]. The side walls of the wedge above the chine are 0.20[m] high. The wedge is equipped with four pressure sensors, positioned along the bottom of the wedge. The positions of the sensors on one side of the wedge are shown in Fig. 17 for the two different deadrise angles. The other two pressure sensors are placed symmetrically at the other side of the wedge. The type of pressure sensor is 113B25 ICP of PCB Piezotronics, with a membrane diameter of 5.54[mm]. This type measures impact pressures accurately during a short time, after which they are 'loaded' and need to 'discharge'. The pressure sensor closest to the tip of the wedge us called pressure sensor 1, the other, closest to the chine, is called 2. The sensors place on the other side of the wedge are used as measure of the variability of the pressure. A sampling frequency of 100[kHz] was used to record the pressure.

Air bubbles in water are created at the bottom of the box. Homogeneity is approximated through the use of sixteen AS23 fresh water air diffusers of Pentair equally distributed along the bottom of the box. The air diffusers create bubbles with varying size in the order of 1[mm] in diameter. The aeration level is measured with the method of Ma et al. [48]. A cylindrical tube is used that is significantly larger than the size of the bubbles. The time it takes to fill the tube with air determines the aeration level. The standard deviation and mean of the aeration levels β_g in the experiment are shown in Fig. 18 for three different locations in the box. The position of the wedge in the box is indicated by the solid black lines near the origin of the horizontal axis. For every location, six aeration measurements are performed and expressed as volume of air over volume of water. The standard deviation of the six aeration measurement increases with increasing level of aeration. It is less than $1 \cdot 10^{-3}$ for the aeration levels approximating 1% by volume, rising to $2.5 \cdot 10^{-3}$ for the aeration levels close to 4% by volume. The variation between locations also increases with increasing level of aeration, being smaller than $3 \cdot 10^{-3}$ for the aeration level close to 1% and rising to more than $1 \cdot 10^{-2}$ for aeration
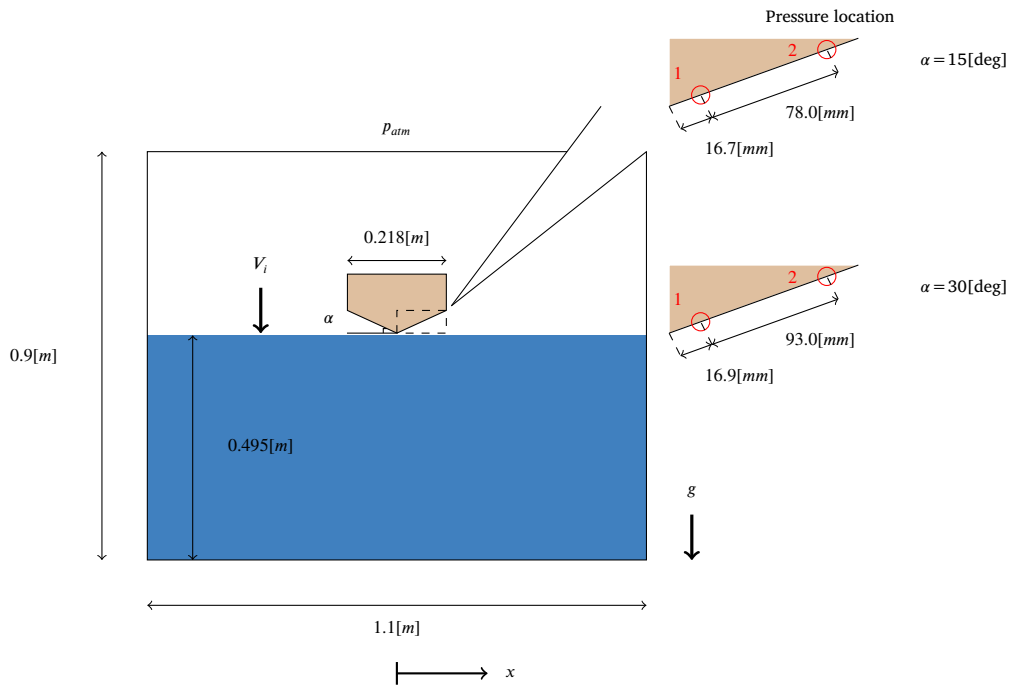
Fig. 17. Setup of wedge impact experiment with aerated water. Dimensions of the experiment are also the dimensions of the numerical domain.
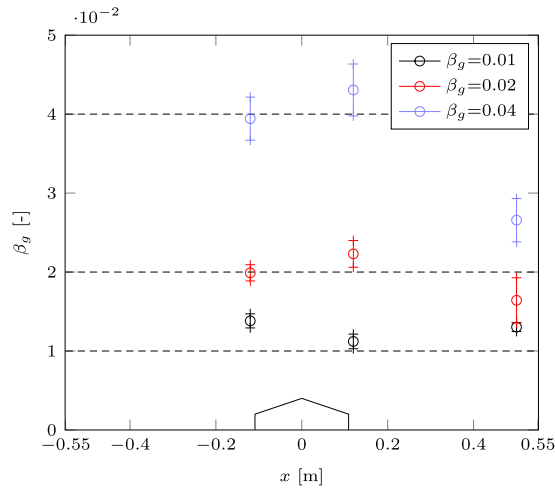

Fig. 18. Aeration measurements represented as air volume over water volume at the free surface for different locations in the box. Position of the wedge is indicated by solid black lines at the bottom of the graph.

levels of 4%. A homogeneous air-water mixture was not achieved, especially considering the aeration levels near the boundary of the box, but near the position of the wedge homogeneity is approximated reasonably well.

The experiment is conducted for combinations of four aeration levels ($\beta_g = 0.0, 0.01, 0.02, 0.04$[-]) and two deadrise angles ($\alpha = 15, 30$[deg]). The impact velocity of the wedge is kept constant at $V_i = 7$[m/s]. The combinations are illustrated with white circles in Fig. 19, showing the edge Mach number as a function of aeration level and deadrise angle. The maximum edge Mach number achieved is $Ma_{edge} = 0.5$. Every test in the experiment is repeated five times and gives 10 data signals as a function time per pressure sensor (recall the symmetrically placed pressure sensors). The 10 data points per time step are used to determine the mean and the standard deviation of the pressure. The expected maximum pressure on the wedge is between 10^4 and 10^7[Pa], so that the density changes in the mixture can be attributed mainly to the air in water [23].
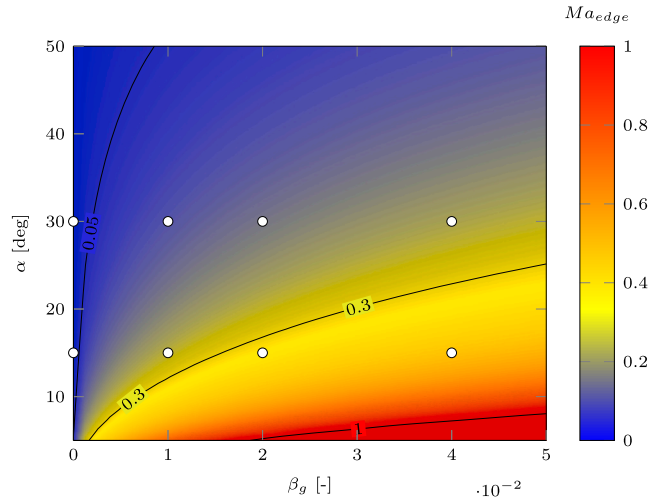
Fig. 19. The edge Mach number (Ma_{edge}) depending on the impact velocity V_i = 7[m/s] and the deadrise angle α of the wedge, and the aeration level β_g for a homogeneous mixture. The experimental tests are represented by ○.

Table 3
Simulation parameters.

Parameter	Value
ρ_l [kg/m^3]	999.00
ρ_a [kg/m^3]	1.22
p_{atm} [Pa]	$1.00 \cdot 10^5$
h_0 [m]	0.01

(a) Initial conditions of fluids and wedge.

Variable	Values			
α [deg]	15		30	
β_g [-]	0.0	0.01	0.02	0.04

(b) Variables considered in the numerical simulations.

7.3. Numerical setup

The size of the domain in the numerical setup is given by Fig. 17. The top boundary of the domain is used to define the atmospheric pressure. The remaining walls are closed and can reflect density waves. The initial height of the bottom of the wedge above the initial waterline h_0 is 10[mm]. The air layer between the wedge and the interface is not expected to affect the loadings as the deadrise angles are too high [21,79].

The relevant parameters for the fluids and wedge are given in Table 3a. The degrees of freedom of the wedge are limited to allow only vertical motion. The end time of the simulations is 0.10[s] so that the entire slamming stage of the interaction between wedge and aerated water is captured. A maximum Courant number of 0.2 is used. The impact velocity of the wedge in the simulations is V_i = 7.0[m/s]. According to the conclusions made for Fig. 10, this allows for solving density wave speeds up to 130[m/s].

Simulations are performed for the same cases in Fig. 19, represented by the white dots, for which tests in the experiment were performed. The relevant parameters are also summarized in Table 3b. These cases cover the range of $0.05 < Ma_{edge} < 0.5$.

A grid convergence test for the simulated pressure is conducted with $\alpha = 15$[deg] and $\beta_g = 0.0$[-]. The dashed box in Fig. 17 is used as a reference for the grid resolution. The reported number of cells therefore is an indication of the number of cells in horizontal and vertical direction used to capture the slope of the bottom of the wedge. The simulation results of the grid convergence test are shown in Fig. 20. The figure shows the pressure obtained at the location of pressure sensor 1 (closest to the tip of the wedge) as solid lines, and the pressure at the location of pressure sensor 2 as dashed lines. The value of the pressure at any time is the average taken over the area of the sensor with diameter 5.54[mm].

The discussion of convergence will focus on pressure sensor 1; the results obtained for pressure sensor two follow a similar trend. One measure of grid convergence is to consider the pressure integrated over time up to 0.005[s], representing an equivalent of impulse. The pressure impulse converges rapidly. The pressure impulse on the finest grid of 135x35 has a value of 487.0[Pa·s]. The difference in pressure impulse with the coarsest grid was 1% of that value; a difference of 0.2% was obtained for 66x29; and a difference of 0.04% for 109x29. Another measure of grid convergence is to consider the maximum pressure during impact. The maximum pressure on the finest grid of 132x35 is $3.7 \cdot 10^5$. The difference in maximum pressure with the coarsest grid of 33x18 is 6.6% of that value. For grid 109x29 the difference in maximum pressure is 2.0% of that value. Grid convergence in terms of the maximum impact pressure therefore has not been obtained. As the convergence is not monotonous, we do not expect that formal grid convergence of the maximum pressure can be obtained. This needs to be accounted for in our interpretation of the comparison between experiment and simulations. All simulations from here on are performed with grid 109x29.
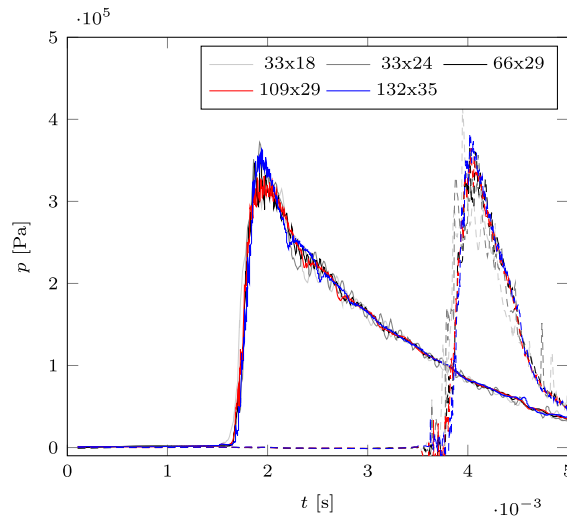
Fig. 20. Simulation results for grid convergence test, using $\alpha = 15$[deg] and $\beta_g = 0.0$[-]. Pressure sensor 1 represented by solid lines. Pressure sensor 2 represented by the dashed lines. Pressure is the average taken over the area of the sensor with diameter 5.54[mm].

7.4. Comparison simulations and experiment: maximum pressures

Fig. 21 shows the pressures obtained from the numerical simulations with grid 109x29 together with the pressures obtained from the tests in the experiment. The atmospheric pressure was subtracted from all results. Solid blue lines are for pressure sensor 1 and dashed blue lines are for pressure sensor 2. The blue lines for the pressure from the experiment are the average of ten signals. A band is formed along the lines representing one standard deviation above and below the average. The lines from the experiment show that discharging the pressure sensors after impact leads to an increased bandwidth around the average pressure and increased uncertainty.

Red lines in Fig. 21 represent the pressures from the simulations, solid lines for pressure sensor 1 and dashed lines for pressure sensor 2. The lines are the average pressures obtained from two simulations at each aeration level β_g with the minimum and maximum value measured at that level on either side of the wedge, see Fig. 18. The following simulations were performed: β_g equals 1.0 and 1.5% for the aeration level of 1.0%; β_g equals 1.9 and 2.4% for a level of 2.0%; β_g equals 3.7 and 4.6% for the aeration level of 4.0%. The uncertainty found from the grid convergence test is not included in Fig. 21.
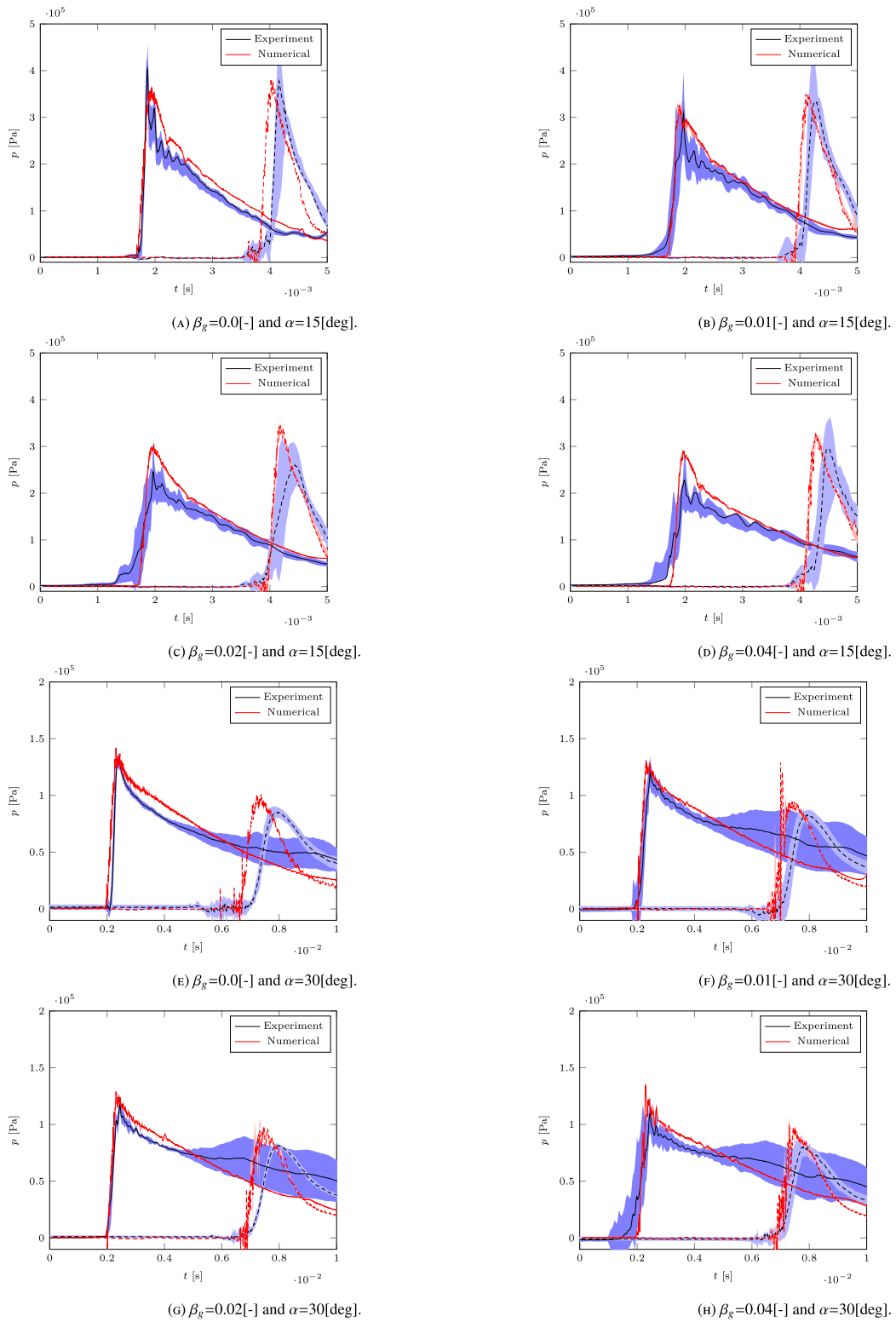
The simulated pressures show good visual agreement with the measured pressures for both deadrise angles and for all aeration levels. The pressures obtained during impacts with the 30[deg] deadrise angle wedge are hardly affected by the level of aeration. This conclusion is consistent between the simulation results and the experimental results. For the wedge with a deadrise angle of 15[deg], the maximum pressure during impact goes down with increasing level of aeration, both in the simulations and in the experiments. There are a number of differences between simulation results and measurements for this wedge. For pressure sensor 2, the pressure in the simulations rises before the pressure in the measurements rises, as if the water reaches pressure sensor 2 earlier in the simulations than it does in the experiments. The most likely explanation is that the jets of water formed by the wedge displacing water are fairly thin, and therefore underresolved in the simulations.

Although the maximum pressure in the measurements can be higher than the pressure in the simulations for some cases, the pressure in the simulations near the maximum pressure is consistently higher. We observed that before for simulations and experiments without aeration, and then it seemed to be due to 3D effects caused by the gaps between wedge and box at both out-of-plane endpoints of the wedge. That is, however, not the only explanation for the difference in pressure between simulations and experiment in this study, because the difference in pressure increases with increasing level of aeration. It seems that the aerated water in the experiments with higher levels of aeration than 1% is more compressible than what is modelled in the simulations.

A final difference that is apparent, is that pressure sensor 1 in the experiment registers a pressure elevation before a pressure is registered in the simulations. That difference in pressure between simulations and experiment before the maximum pressure is attained, becomes larger with increasing levels of aeration. Similar results were found by Elhimer et al. [23] and Ma et al. [47] who explained the difference by a layer of froth at the free water surface that becomes larger with higher levels of aeration. The explanation seems plausible and consistent with what can be observed from Fig. 21, but at present we lack the means to investigate this further.

The pressure maxima in simulations and experiment, with their respective bandwidths, are plotted as a function of level of aeration in Fig. 22. An uncertainty of 2%, as a result of the simulation results not being completely converged for maximum pressures, is included in the graph. Fig. 22 confirms that the level of aeration hardly affects the maximum impact pressures for the wedge with a deadrise angle of 30[deg]. The pressure maxima from the simulations are within the uncertainty band of the experiments, for both wedges at both pressure sensor locations. For the wedge with a deadrise angle of 15[deg], the effect of aeration on the maximum impact pressure is significant. The trends for increasing levels of aeration between simulations and experiment are different. The

(A) β_g=0.0[-] and α=15[deg].

(B) β_g=0.01[-] and α=15[deg].

(C) β_g=0.02[-] and α=15[deg].

(D) β_g=0.04[-] and α=15[deg].

(E) β_g=0.0[-] and α=30[deg].

(F) β_g=0.01[-] and α=30[deg].

(G) β_g=0.02[-] and α=30[deg].

(H) β_g=0.04[-] and α=30[deg].

Fig. 21. Impact pressures: simulation results (red) with experimental results (blue) for two pressure positions. Pressure sensor 1 is represented by solid lines (———). Pressure sensor 2 is represented by dashed lines (– – – ·). Band for the experiments composed of one standard deviation below and one above average pressure. Grid 109×29 was used for the simulations. Simulated pressures are the average of two simulations with the minimum and maximum value for aeration at that level. Band around numerical results formed by minimum and maximum. Uncertainty of grid convergence not included in graphs. (For interpretation of the colors in the figure(s), the reader is referred to the web version of this article.)
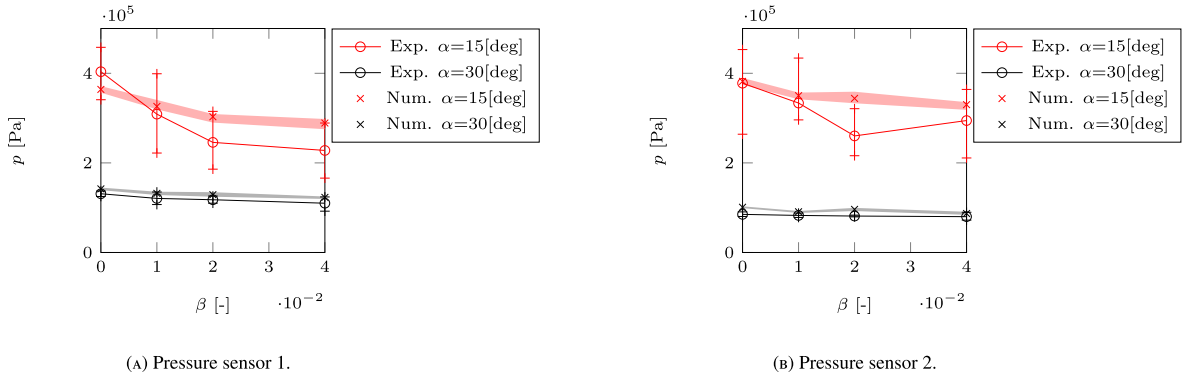
(A) Pressure sensor 1.

(B) Pressure sensor 2.

Fig. 22. Maximum impact pressures for different levels of aeration. Simulation results are compared with experimental result. The band around the experimental pressure maxima is formed by one standard deviation. The filled band around the simulated pressures is formed by the uncertainty due to the grid size and the variation in measured aeration values near each aeration level.
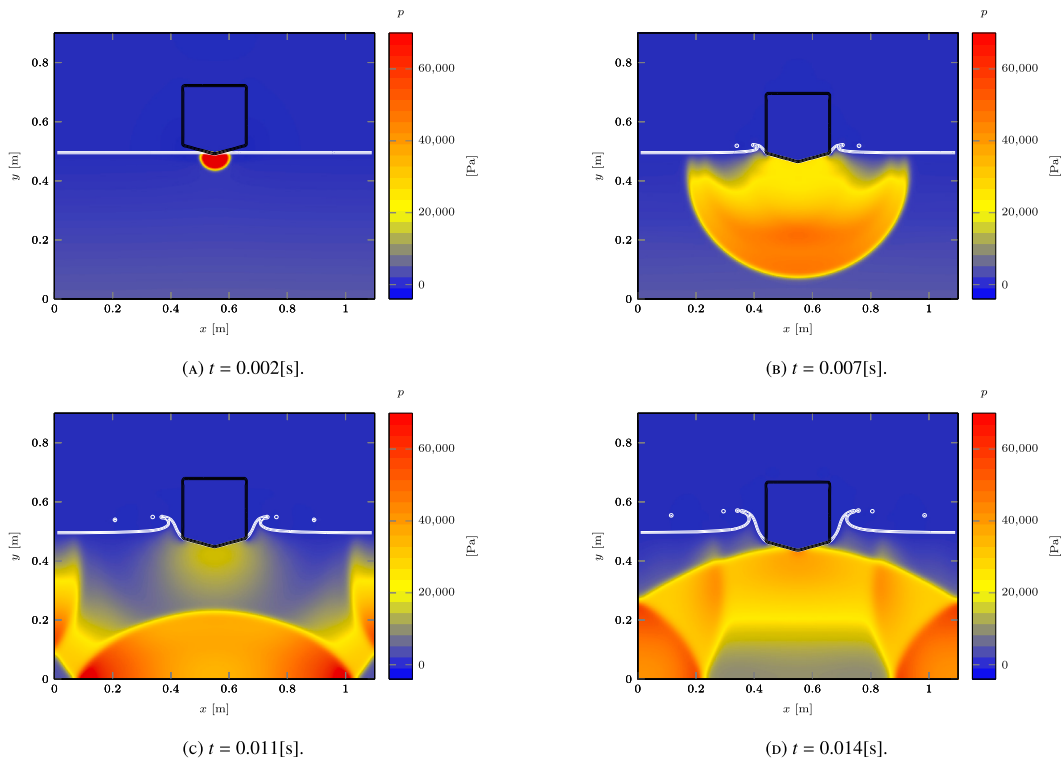

(A) $t = 0.002[s]$.

(B) $t = 0.007[s]$.

(C) $t = 0.011[s]$.

(D) $t = 0.014[s]$.

Fig. 23. Time sequence of simulated pressure fields for wedge impact $\alpha = 15[deg]$ and $\beta_g = 0.04[-]$ at different time instances. From the sequence it becomes apparent that density waves are formed that propagate through the domain. The numerical grid was 109×29.

aerated water in the experiment seems to become more compressible with increasing level of aeration than the modelled air-water mixture in the simulations. This could potentially have to do with the fact that the ratio of air to water for higher levels of aeration is such that bubbles start to influence each other and that the assumption of homogeneity is not valid anymore.

7.5. Comparison simulations and experiment: post-impact pressure oscillations and frequency analysis

The wedge impacting with the aerated water generates density waves due to the compressibility of the air-water mixture. The density waves reflect off of domain boundaries and propagate back to the wedge. The back-and-forth propagation of the density waves causes pressure oscillations on the wedge. A time sequence of the simulated pressure after impact for the wedge with $\alpha = 15[deg]$ and for aerated water with $\beta_g = 0.04[-]$ is shown in Fig. 23. Grid 109x29 was used for the simulation. The density waves become apparent by their front, which shows as a barrier between regions with higher and lower pressure that propagates through the domain.
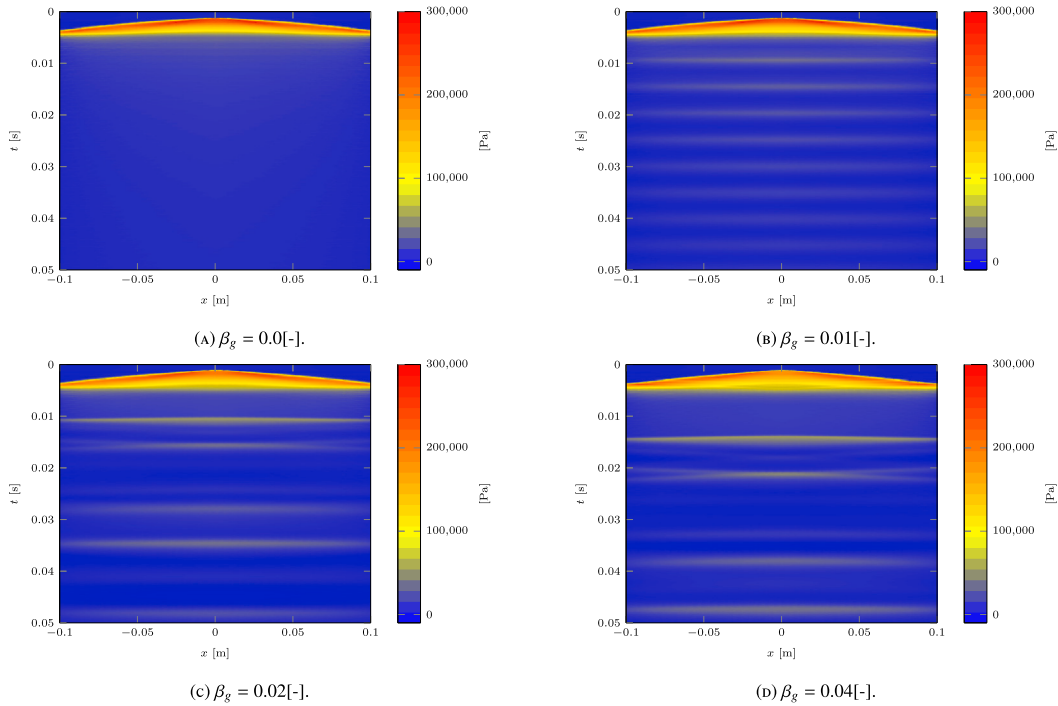
(A) $\beta_g = 0.0$ [-].

(B) $\beta_g = 0.01$ [-].

(C) $\beta_g = 0.02$ [-].

(D) $\beta_g = 0.04$ [-].

Fig. 24. Simulated pressure along bottom of wedge ($\alpha = 15$[deg]) over time for different levels of aeration. Interaction of reflected density waves pressure oscillations on the wedge. Numerical grid used is 109×29.

In Fig. 24, the simulated pressure over time along the chine of the wedge with a deadrise angle of $\alpha = 15$[deg] is shown for four levels of aeration. Grid 109x29 was used for the simulations. In the simulations, an increase in aeration level results in an increase in amplitude of the post-impact pressure oscillations.

The frequency content of the post-impact pressure oscillations was obtained by means of a Fourier analysis of the time signals obtained with the innermost pressure sensor identified as sensor 1 in Fig. 17. Filtered time signals of pressure sensor 1 are shown in Fig. 25 together with the amplitude spectra of the time signals for all considered aeration levels. In order to focus on only the effect of pressure oscillations as a result of density waves, the time signal of the pressure were filtered by means of a band-pass filter that leaves out all frequency content below 40[Hz] and above 400[Hz]. From a hammer test it was found that structural vibrations are higher than 400[Hz]. The pressure oscillations are expected to be caused by reflection of the density waves from the domain boundaries; that means that the frequencies can be predicted by using the speed of sound of the medium together with a typical size of the domain. The speeds of sound of the aerated mixture with aeration levels β_g =0.01, 0.02, 0.04[-] are given by c_f =109, 77, 55[m/s] according to Eq. (24). These velocities are within the mentioned 130[m/s] that can be solved with current Courant number of 0.2.

The expected frequencies of the pressure oscillations can then be found as $f_c = c_f/(2L_d)$, with L_d a typical size of the domain such as the water depth $L_d = h_w = 0.495$[m] or the length of the tip of the wedge to the side walls along the waterline $L_d = x_w = 0.550$[m]. Frequencies f_c associated with horizontal distances and vertical distances have been indicated in Fig. 25 by means of dashed vertical lines. The amplitude spectra are based on time signals that last for h_w/c_f [s] in order to allow at least two pressure cycles to take place, starting from 0.002[s] after the moment the tip of the wedge first touches the free surface. For consistency, the time signals in Fig. 25 show that same time span; the pressure time signals are normalized with the maximum pressure amplitude found in the amplitude spectra, i.e. 10^4 [Pa].

Interestingly, for the experiments with aeration level $\beta_g = 0.0$, an amplitude peak was found with a frequency of around 450[Hz] (not shown in figure). Amplitudes at those frequencies are likely polluted with structural vibrations, but if not they would indicate that there was some air in the water at a level of $\beta_g = 0.0005$). At higher aeration levels, the peaks in the amplitude spectra of the experiment correspond sufficiently well with the predicted frequencies f_c to consider density waves the main explanation for the pressure oscillations and to consider Eq. (24) a good representation of the speed of sound in the mixture. Perfect correspondence cannot be expected when taking into account that the velocity of the wedge causes a Doppler shift, that the distance between pressure sensor 1 and the domain boundaries is not constant and that the density waves undergo constructive and destructive interference. It is also found that the magnitude of the pressure oscillations in the experiments increases by 4% of the maximum impact pressure when comparing β_g =0.01[-] and β_g =0.04[-]. The increase of magnitude with increasing aeration, but not necessarily the percentage itself, is in agreement with the results found in Fig. 23.

When comparing the numerical results with the experimental results, we find that the frequencies f_c of the pressure oscillations, associated with the peaks in the amplitude spectra, are similar between the two. The amplitudes for aeration level $\beta_g = 0.01$[-],
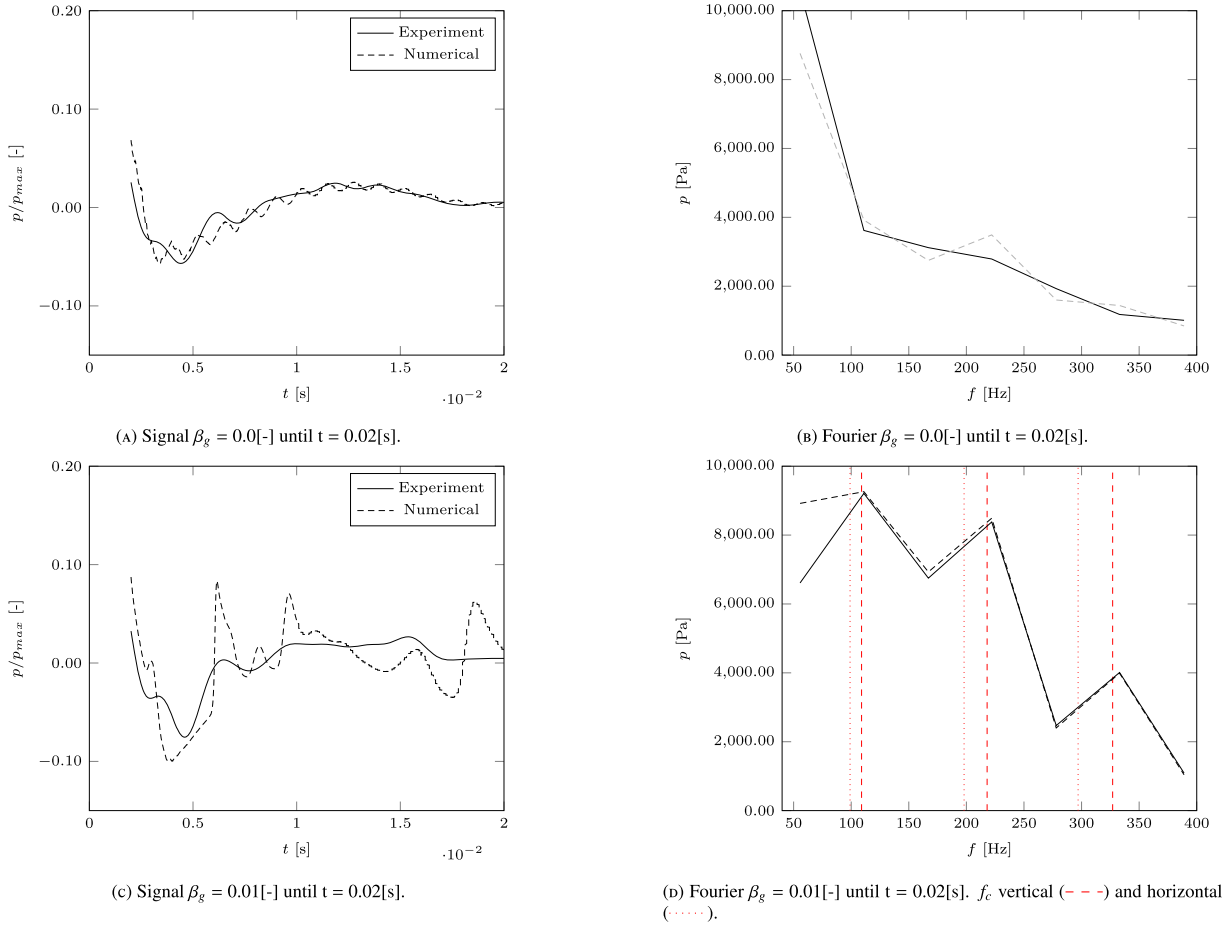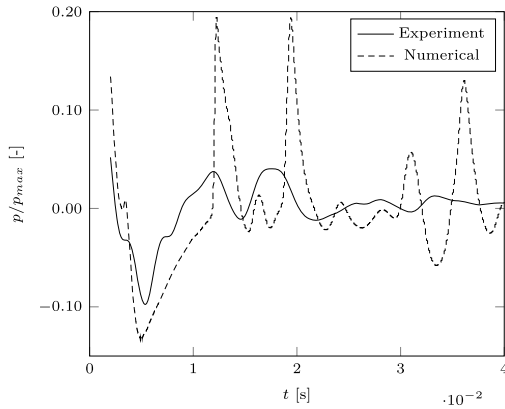
(A) Signal $\beta_g = 0.0$[-] until t = 0.02[s].

(B) Fourier $\beta_g = 0.0$[-] until t = 0.02[s].

(c) Signal $\beta_g = 0.01$[-] until t = 0.02[s].

(D) Fourier $\beta_g = 0.01$[-] until t = 0.02[s]. f_c vertical (- - -) and horizontal ($\cdots$).

Fig. 25. Filtered time signals and amplitude spectra of post-impact pressure oscillations caused by density waves for $\alpha = 15$[deg]. Time signals start 0.002[s] after impact. Band-pass filter between 40 and 400[Hz]). Dashed vertical lines indicate frequencies f_c associated with typical sizes of the domain. The numerical grid used is 109×29.

between simulation and measurement, are nearly identical. The amplitudes of the pressure oscillations also increase for increasing levels of aeration, just like in the experiment, but in the simulations an increase in magnitude of 20% is observed between β_g =0.01[-] and β_g =0.04[-], compared to the 4% in the experiments. For higher levels of aeration, the amplitudes of the pressure oscillations in the simulations are always higher than in the experiment. A potential explanation for the difference between simulations and experiments at higher aeration levels is increased dissipation due to 3D effects near the air bubbles in the water. Further research is necessary to determine whether the assumption of homogeneity of the air-water mixture is justified for aeration levels above β_g = 0.01[-].

8. Conclusion

A new compressible pressure-based multiphase model is presented for modeling the interaction of homogeneous aerated water with moving bodies. It is efficient because the operation that requires most computational effort is solving the Poisson problem for the pressure with a number of unknowns equal to the number of grid cells in the domain. The model can deal with high-density ratio compressible flows using a non-conservative formulation for transport of the interface. The unphysical increase of compressibility, caused by a non-continuous representation of the interface leading to artificial air entrainment, is prevented by means of an additional volume fraction field and a new formulation for the speed of sound.

The numerical results are in good agreement with solutions for traditional compressible multiphase flow cases: an oscillating water piston, a shock tube for separated and dispersed phases, and a cylindrical helium shock bubble. The test cases demonstrate the method's ability to handle contact discontinuities and rarefactions. Geometrical reconstruction of the fluid-fluid and fluid-body interfaces kept these interface sharp. Issues with wiggles around the contact discontinuity were not encountered, because the Courant limit of our formulation depends on the fluid velocities and not on the speed of the density waves. Even with coarse grid resolutions, the pressure levels in propagating density waves were well predicted, but the discontinuity between pressure levels was diffused over a couple of grid cells.
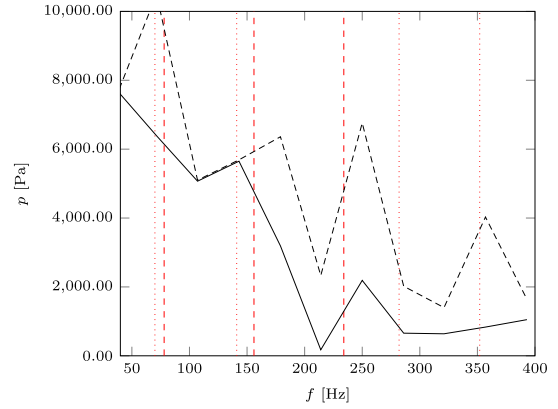
(E) Signal $\beta_g = 0.04[-]$ until t = 0.04[s].
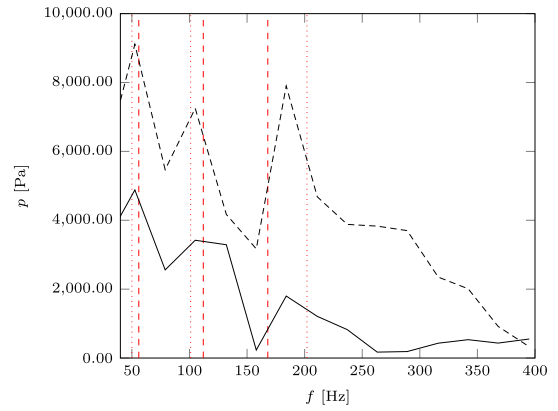
(F) Fourier $\beta_g = 0.04[-]$ until t = 0.04[s]. f_c vertical (– – –) and horizontal (······).
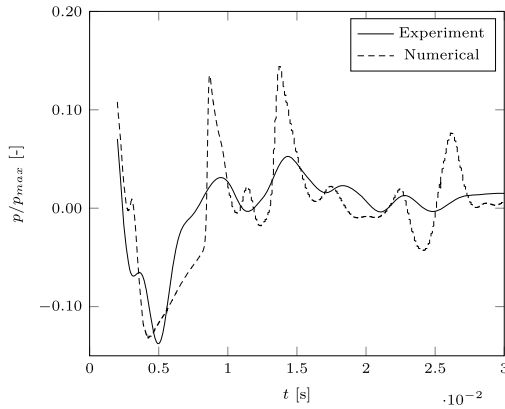
(G) Signal $\beta_g = 0.02[-]$ until t = 0.03[s].

(H) Fourier $\beta_g = 0.02[-]$ until t = 0.03[s]. f_c vertical (– – –) and horizontal (······).

Fig. 25. (*continued*)

A 2D experimental setup for wedge impacts with water was converted specifically for this article to validate the numerical method for the interaction between aerated water and moving bodies in terms of the pressure. Air diffusion stones were placed on the bottom of a box with water to generate aeration levels up to four percent (by volume). We considered Mach numbers of up to 0.5, based on the velocity of the wedge upon impact and the mixture speed of sound. The numerical and experimental results are in good visual agreement for lower aeration levels, both showing a similar maximum pressure and development of the pressure over time. For a deadrise angle of the wedge of 15 degrees the differences at higher aeration levels are larger. For the higher aeration levels, the maximum pressures in the experiment during impact were lower than in the simulations. We believe this to be due to three dimensional effects of the bubbles in the mixture in the experiment at higher aeration levels. These are not accounted for by the numerical model.

The post-impact pressure oscillations due to density waves reflecting from the domain boundaries had higher amplitudes in the simulations than in the experiment. The post-impact oscillation amplitudes become larger with increasing aeration level, up to 4% of the maximum impact pressure in the experiment and up to 20% in the simulations. The governing frequencies of the post-impact oscillations were in good agreement. The speed of sound in the water-air mixture, therefore, is represented well. It is a matter of future study which parts of the numerical method influence the amplitudes of the density waves after impact, so that the method becomes a better representation of the experiment. Overall the assumptions underlying the method are applicable for aeration levels up to 1%.

CRediT authorship contribution statement

Martin van der Eijk: Writing – original draft, Visualization, Validation, Software, Resources, Methodology, Investigation, Formal analysis, Data curation, Conceptualization. **Peter Wellens:** Writing – review & editing, Writing – original draft, Visualization, Validation, Supervision, Software, Resources, Project administration, Methodology, Investigation, Formal analysis, Data curation, Conceptualization.

Declaration of competing interest

The authors declare that they have no known competing financial interests or personal relationships that could have appeared to influence the work reported in this paper.

Data availability

Data will be made available on request.

Acknowledgements

References

[1] R. Abgrall, S. Karni, Computations of compressible multifluids, J. Comput. Phys. 169 (2001) 594–623.
[2] M. Ansari, A. Daramizadeh, Numerical simulation of compressible two-phase flow using a diffuse interface method, Int. J. Heat Fluid Flow 42 (2013) 209–223.
[3] J.W. Banks, W.D. Henshaw, D.W. Schwendeman, An analysis of a new stable partitioned algorithm for fsi problems. Part II: incompressible flow and structural shells, J. Comput. Phys. 268 (2014) 399–416.
[4] M.A.I. Branch, Report on the investigation of the structural failure of msc Napoli English channel on 18 January 2008, Report, Marine Accident Investigation Branch, London, 2007.
[5] H. Bredmose, G. Bullock, A. Hogg, Violent breaking wave impacts. Part 3. Effects of scale and aeration, J. Fluid Mech. 765 (2015) 82–113.
[6] H. Bredmose, D. Peregrine, G. Bullock, Violent breaking wave impacts. Part 2: modelling the effect of air, J. Fluid Mech. 641 (2009) 389–430.
[7] G. Bullock, A. Crawford, P. Hewson, M. Walkden, P. Bird, The influence of air and scale on wave impact pressures, Coast. Eng. 42 (2001) 291–312.
[8] G. Bullock, C. Obhrai, D. Peregrine, H. Bredmose, Violent breaking wave impacts. Part 1: results from large-scale regular wave tests on vertical and sloping walls, Coast. Eng. 54 (2007) 602–617.
[9] M. Bussmann, D.B. Kothe, J.M. Sicilian, Modeling high density ratio incompressible interfacial flows, in: ASME 2002 Joint US-European Fluids Engineering Division Conference, American Society of Mechanical Engineers Digital Collection, 2002, pp. 707–713.
[10] P. Carrica, D. Drew, F. Bonetto, R. Lahey Jr, A polydisperse model for bubbly two-phase flow around a surface ship, Int. J. Multiph. Flow 25 (1999) 257–305.
[11] A.M. Castro, P.M. Carrica, Eulerian polydispersed modeling of bubbly flows around ships with application to athena r/v, Int. Shipbuild. Prog. 60 (2013) 403–433.
[12] A.M. Castro, J. Li, P.M. Carrica, A mechanistic model of bubble entrainment in turbulent free surface flows, Int. J. Multiph. Flow 86 (2016) 35–55.
[13] Y. Cheny, O. Botella, The ls-stag method: a new immersed boundary/level-set method for the computation of incompressible viscous flows in complex moving geometries with good conservation properties, J. Comput. Phys. 229 (2010) 1043–1076.
[14] A.J. Chorin, Numerical solution of the Navier-Stokes equations, Math. Comput. 22 (1968) 745–762.
[15] S.T. Dang, E.A. Meese, J.C. Morud, S.T. Johansen, Numerical approach for generic three-phase flow based on cut-cell and ghost fluid methods, Int. J. Numer. Methods Fluids 91 (2019) 419–447.
[16] F. Dias, L. Brosset, Comparative numerical study: description of the calculation case, in: 20th Int. Offshore and Polar Eng. Conf., 2010.
[17] F. Dias, D. Dutykh, J.M. Ghidaglia, A two-fluid model for violent aerated flows, Comput. Fluids 39 (2010) 283–293.
[18] B. Duret, R. Canu, J. Reveillon, F. Demoulin, A pressure based method for vaporizing compressible two-phase flows with interface capturing approach, Int. J. Multiph. Flow 108 (2018) 42–50.
[19] M. van der Eijk, P. Wellens, An efficient bilinear interface reconstruction algorithm and consistent multidimensional unsplit advection scheme for accurate capturing of highly-curved interfacial shapes on structured grids, J. Comput. Phys. 498 (2024) 112656.
[20] M. van der Eijk, P.R. Wellens, A compressible two-phase flow model for pressure oscillations in air entrapments following green water impact events on ships, Int. Shipbuild. Prog. (2020) 1–29.
[21] M. van der Eijk, P.R. Wellens, Experimental and numerical assessment of vertical accelerations during bow re-entry of a rib in irregular waves, Int. Shipbuild. Prog. 67 (2020) 173–198.
[22] M. van der Eijk, P.R. Wellens, Two-phase free-surface flow interaction with moving bodies using a consistent, momentum preserving method, J. Comput. Phys. 474 (2023) 111796, https://doi.org/10.1016/j.jcp.2022.111796.
[23] M. Elhimer, N. Jacques, A.E.M. Alaoui, C. Gabillet, The influence of aeration and compressibility on slamming loads during cone water entry, J. Fluids Struct. 70 (2017) 24–46.
[24] V. Eroshin, A. Plyusnin, N. Romanenkov, Y.A. Sozonenko, Y.L. Yakimov, Influence of the atmosphere on the magnitude of the hydrodynamic forces in the case of a disk in a flat encounter with the surface of a compressible liquid, Fluid Dyn. 19 (1984) 350–355.
[25] G. Fekken, Numerical simulation of free-surface flow with moving rigid bodies, Ph.D. thesis, Delft University of Technology, 2004.
[26] E. Franquet, Modélisation eulérienne d'écoulements multiphasiques en présence d'ondes de chocs, de détonations et d'interfaces matérielles. Application aux matériaux énergétiques nanostructurés, Ph.D. thesis, 2006.
[27] M. Greco, O. Faltinsen, M. Landrini, Shipping of water on a two-dimensional structure, J. Fluid Mech. 525 (2005) 309–332.
[28] M. Greenhow, Wedge entry into initially calm water, Appl. Ocean Res. 9 (1987) 214–223.
[29] P.M. Gresho, R.L. Lee, Don't suppress the wiggles—they're telling you something!, Comput. Fluids 9 (1981) 223–253.
[30] P.M. Guilcher, G. Oger, E. Jacquin, L. Brosset, N. Grenier, D. Le Touzé, Simulation of liquid impacts with a two-phase parallel sph model, in: The Twentieth International Offshore and Polar Engineering Conference, OnePetro, 2010.
[31] J.F. Haas, B. Sturtevant, Interaction of weak shock waves with cylindrical and spherical gas inhomogeneities, J. Fluid Mech. 181 (1987) 41–76.
[32] M. Hattori, A. Arami, T. Yui, Wave impact pressure on vertical walls under breaking waves of various types, Coast. Eng. 22 (1994) 79–114.
[33] C. Hirsch, Numerical Computation of Internal and External Flows: The Fundamentals of Computational Fluid Dynamics, Butterworth-Heinemann, 2007.
[34] Y. Hong, B. Wang, H. Liu, Aeration effects on hydrodynamic loads of circular cylinder's high-speed water entry, Int. J. Offshore Polar Eng. 29 (2019) 446–451.
[35] Y. Hong, B. Wang, H. Liu, Numerical study of hydrodynamic loads at early stage of vertical high-speed water entry of an axisymmetric blunt body, Phys. Fluids 31 (2019) 102105.
[36] Y. Hong, B. Wang, H. Liu, Experimental and numerical study on hydrodynamic impact of a disk in pure and aerated water, Proc. Inst. Mech. Eng., Part M, J. Eng. Marit. Environ. 235 (2021) 152–164.

[37] W. Huang, H. Xiao, Numerical modeling of dynamic wave force acting on Escambia Bay bridge deck during Hurricane Ivan, J. Waterw. Port Coast. Ocean Eng. 135 (2009) 164–175.

[38] E. Johnsen, T. Colonius, Implementation of weno schemes in compressible multicomponent flow problems, J. Comput. Phys. 219 (2006) 715–732.

[39] A. Kapila, R. Menikoff, J. Bdzil, S. Son, D.S. Stewart, Two-phase modeling of deflagration-to-detonation transition in granular materials: reduced equations, Phys. Fluids 13 (2001) 3002–3024.

[40] J. Kay, Uk storms destroy railway line and leave thousands without power, See http://www.bbc.co.uk/news/uk-26042990, 2014.

[41] K. Kleefsman, G. Fekken, A. Veldman, B. Iwanowski, B. Buchner, A volume-of-fluid based simulation method for wave impact problems, J. Comput. Phys. 206 (2005) 363–393.

[42] A. Korobkin, Analytical models of water impact, Eur. J. Appl. Math. 15 (2004) 821–838.

[43] J.J. Kreeft, B. Koren, A new formulation of Kapila's five-equation model for compressible two-fluid flow, and its numerical treatment, J. Comput. Phys. 229 (2010) 6220–6242.

[44] U. Laur, K. Lehtola, A. Eksborh, Final report on the capsizing on 28 September 1994 in the Baltic Sea of the ro-ro passenger vessel mv Estonia, Final Report, ISBN 951-53-1611-1, 1997.

[45] B. Leonard, A. Lock, M. MacVean, Conservative explicit unrestricted-time-step multidimensional constancy-preserving advection schemes, Mon. Weather Rev. 124 (1996) 2588–2606.

[46] S. Liu, I. Gatin, C. Obhrai, M.C. Ong, H. Jasak, Cfd simulations of violent breaking wave impacts on a vertical wall using a two-phase compressible solver, Coast. Eng. 154 (2019) 103564.

[47] Z. Ma, D. Causon, L. Qian, C. Mingham, H. Gu, P.M. Ferrer, A compressible multiphase flow model for violent aerated wave impact problems, in: Proceedings of the, Royal Society of London A: Mathematical, Physical and Engineering Sciences, The Royal Society, 2014, p. 20140542.

[48] Z. Ma, D. Causon, L. Qian, C. Mingham, T. Mai, D. Greaves, A. Raby, Pure and aerated water entry of a flat plate, Phys. Fluids 28 (2016) 016104.

[49] T. Mai, C. Mai, A. Raby, D. Greaves, Aeration effects on water-structure impacts: part 1. Drop plate impacts, Ocean Eng. 193 (2019) 106600.

[50] T. Mai, C. Mai, A. Raby, D. Greaves, Aeration effects on water-structure impacts: part 2. Wave impacts on a truncated vertical wall, Ocean Eng. 186 (2019) 106053.

[51] S. Miller, H. Jasak, D. Boger, E. Paterson, A. Nedungadi, A pressure-based, compressible, two-phase flow finite volume method for underwater explosions, Comput. Fluids 87 (2013) 132–143.

[52] A. Murrone, H. Guillard, A five equation reduced model for compressible two phase flow problems, J. Comput. Phys. 202 (2005) 664–698.

[53] V.T. Nguyen, W.G. Park, A free surface flow solver for complex three-dimensional water impact problems based on the vof method, Int. J. Numer. Methods Fluids 82 (2016) 3–34.

[54] D. Peregrine, H. Bredmose, G. Bullock, C. Obhrai, G. Müller, G. Wolters, Violent water wave impact on a wall, in: Proceedings of 14th Aha, Huliko Winter Workshop, Honolulu, Hawaii, 2005.

[55] D. Peregrine, L. Thais, The effect of entrained air in violent water wave impacts, J. Fluid Mech. 325 (1996) 377–397.

[56] L.R. Plumerault, D. Astruc, P. Maron, The influence of air on the impact of a plunging breaking wave on a vertical wall using a multifluid model, Coast. Eng. 62 (2012) 62–74.

[57] L.R. Plumerault, D. Astruc, P. Villedieu, P. Maron, A numerical model for aerated-water wave breaking, Int. J. Numer. Methods Fluids 69 (2012) 1851–1871.

[58] J.J. Quirk, S. Karni, On the dynamics of a shock–bubble interaction, J. Fluid Mech. 318 (1996) 129–163.

[59] M. Raessi, H. Pitsch, Consistent mass and momentum transport for simulating incompressible interfacial flows with large density ratios using the level set method, Comput. Fluids 63 (2012) 70–81.

[60] J. Roenby, S. Aliyar, H. Bredmose, A robust algorithm for computational floating body dynamics, R. Soc. Open Sci. 11 (2024) 231453.

[61] R. Saurel, R. Abgrall, A multiphase Godunov method for compressible multifluid and multiphase flows, J. Comput. Phys. 150 (1999) 425–467.

[62] R. Saurel, F. Petitpas, R.A. Berry, Simple and efficient relaxation methods for interfaces separating compressible fluids, cavitating flows and shocks in multiphase mixtures, J. Comput. Phys. 228 (2009) 1678–1712.

[63] S. Schenke, T.J. van Terwisga, An energy conservative method to predict the erosive aggressiveness of collapsing cavitating structures and cavitating flows from numerical simulations, Int. J. Multiph. Flow 111 (2019) 200–218.

[64] J.C. Scott, The role of salt in whitecap persistence, in: Deep Sea Research and Oceanographic Abstracts, Elsevier, 1975, pp. 653–657.

[65] K. So, X. Hu, N.A. Adams, Anti-diffusion interface sharpening technique for two-phase compressible flow simulations, J. Comput. Phys. 231 (2012) 4304–4323.

[66] G.A. Sod, A survey of several finite difference methods for systems of nonlinear hyperbolic conservation laws, J. Comput. Phys. 27 (1978) 1–31.

[67] R. Verstappen, A. Veldman, Symmetry-preserving discretization of turbulent flow, J. Comput. Phys. 187 (2003) 343–368.

[68] T. Von Karman, The impact on seaplane floats during landing, 1929.

[69] T.V. Vu, S. Homma, G. Tryggvason, J.C. Wells, H. Takakura, Computations of breakup modes in laminar compound liquid jets in a coflowing fluid, Int. J. Multiph. Flow 49 (2013) 58–69.

[70] H. Wagner, Über stoß- und gleitvorgänge an der oberfläche von flüssigkeiten, Z. Angew. Math. Mech. (Zeitschrift für Angewandte Mathematik und Mechanik) 12 (1932) 193–215.

[71] K. Wei, J. Hong, M. Jiang, W. Zhao, A review of breaking wave force on the bridge pier: experiment, simulation, calculation, and structural response, J. Traffic Transp. Eng. (Engl. Ed.) (2022), https://doi.org/10.1016/j.jtte.2021.03.006, https://www.sciencedirect.com/science/article/pii/S2095756422000150.

[72] R. Wemmenhove, Numerical Simulation of Two-Phase Flow in Offshore Environments, University Library Groningen[Host], 2008.

[73] G.D. Weymouth, D.K.P. Yue, Conservative volume-of-fluid method for free-surface simulations on Cartesian-grids, J. Comput. Phys. 229 (2010) 2853–2865.

[74] P.S. Wilson, R.A. Roy, An audible demonstration of the speed of sound in bubbly liquids, Am. J. Phys. 76 (2008) 975–981.

[75] A. Wood, A Textbook of Sound, Bell, London, 1941, 578 pp.

[76] D.J. Wood, D.H. Peregrine, T. Bruce, Wave impact on a wall using pressure-impulse theory. I: trapped air, J. Waterw. Port Coast. Ocean Eng. 126 (2000) 182–190.

[77] Z. Xie, T. Stoesser, A three-dimensional Cartesian cut-cell/volume-of-fluid method for two-phase flows with moving bodies, J. Comput. Phys. 416 (2020) 109536.

[78] R. Zhao, O. Faltinsen, Water entry of two-dimensional bodies, J. Fluid Mech. 246 (1993) 593–612.

[79] X. Zhu, O.M. Faltinsen, C. Hu, Water entry and exit of a horizontal circular cylinder, 2007.